Original Research Article

An elastic-plastic finite element analysis of two interfering hemispheres sliding in frictionless contact

Abstract

A vast amount of previous work on hemispherical contact is almost solely dedicated to quasi-static normal loading (axisymmetric 2D models). Some scarce work exists on tangential loading but limited to full stick conditions. Sliding of interfering bodies is considerably distinct. Hence, the objective of this work is to investigate two hemispheres sliding across each other, subject to an interference that is large enough to deform their surfaces permanently, during and after contact. Similar (steel-on-steel) and dissimilar (aluminum-on-copper) materials are investigated using a 3D finite element analysis (FEA). The behavior and outcomes *are vastly different* from previously reported work. Results include the formation and propagation of the von Mises stresses, the deformations, the contact areas, and the energy loss even with friction being absent. The results are normalized so that they may be applied to any scale (from macro to micro contacts), with an intent to apply the results to interfering asperities in rough surfaces sliding. The effectiveness of that normalization is discussed. Empirical equations for the net energy loss, the permanent residual deformations (damage), and the effective coefficient of friction (in frictionless sliding) are given as functions of the interference. Lastly, some FEA results are favorably compared to those obtained from a semi-analytical method, but only limited to a few special cases that the latter is capable to solve.

Keyword: Tribology; contact mechanics; interference sliding; large deflections; plasticity; post sliding residual stresses and deformations; effective friction; energy loss.

1. Introduction

This work presents results from a three dimensional (3D) finite element analysis (FEA) of an elastic-plastic asperity contact model for two hemispherical bodies *sliding across each other* with various preset vertical interferences. Sliding contact is an important phenomenon in both the macro and micro scales. In the macro scale, it is important to consider friction, wear, and residual deformation that occur when interfering surfaces slide across each other, e.g., rolling element bearings, gears, cams, etc. In the micro scale, it is well known that nominally smooth surfaces have undulations in their surface profile and the true area of contact is just a small fraction of the nominal area of contact. These high points, or asperities, are known to deform plastically during sliding. Three dimensional sliding of a pair of asperities provides the kernel of the solution for any stochastically distributed rough surface. Thus, it is important to know how the deformed geometry, residual stresses, and surface condition affect the sliding process between a pair of asperities. The model presented here has been normalized in order to apply the results to both macro and micro scale geometries.

Liu et al. [1] review early work done over the years dealing with elastic and elastic-plastic contact that are based on the contact of a single asperity expanded in a statistical model for multiple asperity contact, and share the common methodology of Thomas [2], and Greenwood [3]. Some of these works are restricted to the elastic regime, such as the landmark work by Greenwood and Williamson [4]. Other works [5-9] extend the Greenwood and Williamson model in the elastic regime to a variety of geometries and different basic assumptions. Other works concentrate on purely plastic

deformation, and are based on the models of Abbott and Firestone [10], and Tsukizoe and Hisakado [8].

Normal spherical contacts have been massively investigated, e.g., Evseev et al. [11], Chang [12], and Zhao [13]. FEA has been used by Vu-Quoc et al. [14] to analyze normal contact between two spheres, which by symmetry is equivalent to that of one sphere in contact with a rigid flat. Adams and Nosonovsky [15] provide a review of contact modeling with an emphasis on the contact forces . Jackson and Green [16], and Wang and Keer [17] explored hemispherical elastic-plastic contact in a normal loading conditions. *However, the characteristics of normal contact as opposed to sliding contact are very different and, thus, the latter is the impetus of this work.*

Some work has been done in the area of sliding spherical contact, but in most cases either simplifying assumptions have ignored important phenomena or less than satisfactory results have been produced. There have been many works, mainly based on Green [18, 19], which analyzed friction and adhesion of triangular shaped contact geometries. In reality though, the contact junctions are more realistically modeled as spherical in shape. Faulkner and Arnell [20] present the first work that models sphere-on-sphere sliding contact using an FEA approach. No general results are presented in that work and the method resulted in extremely long execution times (over 960 hours). A semi-analytical approach is given by Jackson et al. [21] heuristically applying the normal contact model in [16].

More recent studies report results of fretting cycles [22 – 25]. The elastic-plastic and fully plastic spherical contacts in strictly normal loading have been studied in great details, using the finite element analysis (FEA) method [24-28].The elastic-plastic

cylindrical contact in plane stress is recently examined by Sharma [29]. However, when tangential force is introduced under normal load, few attempts to analyze the contact have been made. Brizmer et al. [30] use the finite element method to investigate the spherical contact under full stick condition subject to a tangential load. Chang and Zhang [31] model their contact without the fully stick conditions but apply a static frictional coefficient. The work by Vijaywargiya and Green [32] presents the results of a finite element analysis used to simulate two-dimensional (2D) sliding between two interfering elastic-plastic cylinders. The work by Boucly et al. [33] presents another semi-analytical method (SAM) for the tridimensional elastic-plastic sliding contact between two hemispherical asperities using either load-driven or a displacement-driven algorithms (that model shall be compared to within). Gupta et al. [34] develop a model that consists of a meager 285 elements. Ghosh et al. [35] simulates the fretting wear of Hertzian line contact in partial slip. Another recent work [36] analyzes the contact between a hemisphere and a rigid flat block in full stick condition, while a very recently work [37] studies fretting sliding but of a cylinder in contact with a flat block.

It is concluded that none of the previous works investigates the sliding phenomenon between two interfering hemispheres as reported herein. This work adopts the kinematics defined in [32] but applied to 3D modelling necessitated by hemispherical sliding. With current computing capabilities, the accuracy of the results can be improved considerably and that is one of the aims of this work. First, modeling is performed with sufficiently fine and adaptive meshes that capture the behavior in the contact region with great accuracy. Then, results are reported in a non-dimensional form to allow their broader utility.

Hertzian theory suggests that two elastic bodies in contact can be modeled as an equivalent ellipsoid pressed against a rigid flat. Such an equivalent model has no physical grounds or mathematical proof once plasticity takes place, certainly not when the two sliding bodies have distinct material properties. In this work, individual elastic-plastic hemispheres sliding over each other are treated, and not as a part of a statistically generated surface. Sliding is simulated by means of FEA wherein the two interfering bodies are both fully modeled, without resorting to the common model of an equivalent body against a flat. This is particularly important when sliding takes place between dissimilar materials. This work is then compared to a novel semi-analytical technique developed by Boucly et al [33].

In the elastic domain, up to the onset of plasticity, the Hertzian solution is used to obtain critical values of load, contact half-width, and strain energy as defined in Green [22]. As shown in [16, 27], hardness is not a unique material property because it varies with the deformation as well as with other material properties (i.e., yield strength, Poisson's ratio, and the elastic modulus). Instead, the method and definitions outlined in [22] are adopted. While the said analysis pertains to normal loading, the critical values are useful for results normalization herein just as well. The foregoing is a brief summary. Using the distortion energy yield criterion at the site of maximum von Mises stress, and letting $\left[\sigma_e\right]_{\max} = S_y$, where S_y is the yield strength, results in the critical values of force, P_c, contact area, A_c, and interference, ω_c. These are given by [38]:

$$P_c = \frac{(\pi C S_y)^3 \mathrm{R}^2}{6E'^2} \quad , A_c = \frac{\pi^3 \left(C S_y R\right)^2}{\left(2E'\right)^2} \quad , \omega_c = \left(\frac{C S_y}{2E'}\right)^2 R \, , \tag{1}$$

The von Mises stress, σ_e, normalized by the maximum pressure, p_o, is a function of the depth normalized by the contact radius, ζ, where Poisson's ratio, ν, is a parameter [38]:

$$\frac{\sigma_e}{p_o} = \frac{1}{2}\sqrt{\frac{\left[(1-2\nu-2\zeta^2(1+\nu)+2(\zeta+\zeta^3)(1+\nu)arccot(\zeta)\right]^2}{(1+\zeta^2)^2}}. \quad (2)$$

The equivalent radius, R, and equivalent modulus of elasticity, E', are calculated by:

$$\frac{1}{R} = \frac{1}{R_1} + \frac{1}{R_2}, \quad (3)$$

$$\frac{1}{E'} = \frac{1-\nu_1^2}{E_1} + \frac{1-\nu_2^2}{E_2}, \quad (4)$$

The value ζ_c is the nondimensional depth where Eq. (2) is maximum, while C is the reciprocal of Eq. (2). Both are functions of the Poisson ratio alone:

$$\zeta_c(\nu) = 0.38167 + 0.33136\nu, \quad (5)$$

$$C(\nu) = 1.30075 + 0.87825\nu + 0.54373\nu^2. \quad (6)$$

However, because at yielding $\left[\sigma_e\right]_{\max} = S_y$, it is the product of CS_y that is to be used in Eq. (1). For dissimilar materials (as is the case herein), depending on which material yields first, this product is determined by [38]:

$$CS_y = \min(CS_{y1}, CS_{y2}). \quad (7)$$

Likewise, the maximum elastic energy that can possibly be stored (up to the point of yielding onset) is [22]:

$$U_c = \frac{\pi\left(CS_y\right)^5 R^3}{60E'^4}. \quad (8)$$

All quantities herein are subsequently being normalized by the critical parameters calculated from Eqs. (1-8). Thus, the ensuing results apply for any geometry scale as long

as continuum mechanics is assumed to prevail; therefore, the radii for the hemispheres in the FE model are subjectively chosen to be $R_1 = R_2 = 1m$.

This analysis considers both steel-on-steel and aluminum-on-copper contact. For the steel-on-steel case the critical values are calculated for identical material properties as follows: $\mathrm{E}_1 = \mathrm{E}_2 = 200\,\mathrm{GPa}$, $\nu_1 = \nu_2 = 0.32$, and $S_y = 0.9115\,\mathrm{GPa}$. This material has its yield strength in the middle of the range of the five steel materials investigated by Jackson et al. [23]. While the results obtained in this work are not representative of all steel materials, because of the normalization proposed herein, this case may be extended to any two identical materials. The aluminum-on-copper hemispheres are modeled by sliding of a hemisphere made of a copper-based metal matrix composite (MMC) alloy known commercially as Glidcop-Al25 over an Al 6061-T651 hemisphere. These particular materials are chosen here because of their specific use in an electromagnetic accelerator. Table 1 presents the material properties used in this analysis, and Table 2 presents the critical values calculated from the above equations (1-8). Notably by comparison copper is stiffer and stronger than aluminum (which impacts the behavior and it shall be apparent in the forthcoming results). Table 3 presents the interferences for all the cases studied for both steel-on-steel and aluminum-on-copper. All materials are regarded as elastic-perfectly plastic, but in order to help convergence, a bi-linear material model with a 2% strain hardening based on the elastic modulus is used. This small amount of strain hardening has been verified to not significantly affect the forthcoming results yet drastically improves upon convergence time.

Table 1: Material properties for the hemispheres (from MatWeb)

Property	Steel	Aluminum	Copper
E	200 GPa	68.0 GPa	130 GPa
S_y	911.5 MPa	310 MPa	331 MPa
υ	0.32	0.326	0.33

Table 2: Critical values of parameters at the onset of plasticity for sliding between two hemispherical contacts

Parameter	Steel-on-Steel	Al-on-Cu*
CS_y	1.493 GPa	509.9 MPa
ω_c	0.2214 mm	0.1261 mm
P_c	346.1 kN	67.32 kN
A_c	347.8 mm^2	198 mm^2
U_c	30.65 J	3.395 J

*Aluminum yields first

Table 3: The interferences, ω, for all cases presented in this analysis.

	Interference, ω [mm]					
$\omega^* = \omega / \omega_c$	2	4	6	9	12	15
Steel-on-Steel	0.4428	0.8856	1.328	1.993	2.657	3.321
Aluminum-on-Copper	0.2522	0.5044	0.7566	1.135	1.513	1.892

2. Modeling Method

Figure 1 shows a schematic representation of the sliding process along with the coordinate system (x,y). The definitions are identical to those presented to model interfering cylinders in sliding (Vijaywargiya and Green [24]). In this analysis a displacement, Δx, is applied to the top surface of the top hemisphere where the bottom surface of the bottom hemisphere is held stationary. This Δx represents the total horizontal sliding distance that a hemisphere must slide side-to-side in order to complete a single-pass sliding contact. The total sliding distance is calculated from geometry and it is a function of the vertical interference, ω, where Δx increases with the preset interference ω. That total distance is divided into n equal load steps, $\delta x = \Delta x / n$. Hence, at load step i the horizontal location of the center of the moving hemisphere relative to the center of the stationary hemisphere is:

$$x = i \cdot \delta x - \frac{\Delta x}{2}; \quad i = 0, n + m$$

Because of material tugging m load steps are added to ensure exit from sliding contact. Normalizing x by R, the loading phase is defined by the region $x/R<0$, where the top hemisphere is pressed horizontally against the bottom one before passing the vertical axis of alignment ($x/R=0$). The unloading phase is defined in the region $x/R>0$, where the top hemisphere has passed the vertical axis of alignment, and where the hemispheres are expected to repel each other, and ultimately disengage.

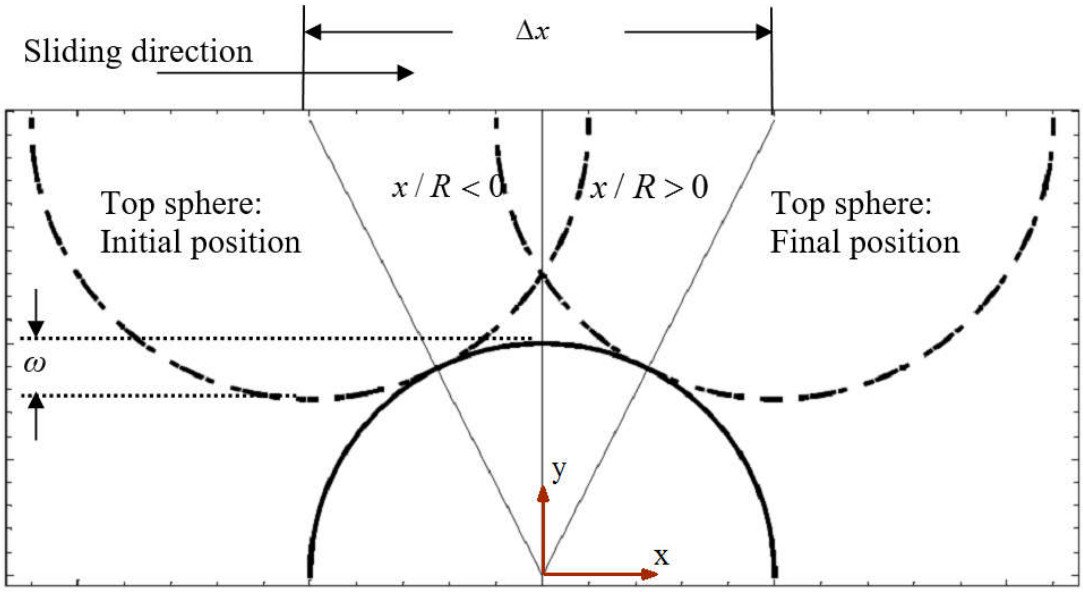

Figure 1: The schematic of the sliding process of two interfering hemispheres

2.1 Assumptions

Following are the assumptions that are used to simplify the problem:

1) Herein sliding is assumed to be a frictionless process, and hence no coefficient of friction is input in the FE model. This is done in order to isolate the effect of plasticity during sliding.
2) It is assumed that the mesh validated up to the onset of plasticity is also robust for analysis of the elastic-plastic regime, since no closed form solution is available beyond that point for this purpose. [Worthy of note, the mesh is continually adjusted for various vertical interferences as necessary (see below).]
3) This work concentrates on the area close to the contact surfaces and far field bulk deformation effects are assumed not to have a significant effect on the region close to the contact surfaces (Saint Venant's principle).

4) Sliding is simulated as a quasi-static process, i.e., time-dependent phenomena are not analyzed. Hence, dynamic effects are ignored and material properties used do not depend on the strain rate. Likewise, adhesion and stick-slip phenomena are not accounted for.
5) Temperature effects that might occur during sliding are not considered, and the material properties used are assumed to be at room temperature and constant.

This analysis is done using ABAQUS, a commercial FEA software package using linear brick (8-node) elements. A representative model is presented in Figure 2. In order to take advantage of the symmetry of the problem, each sphere is cut in half along the vertical plane. Because the spheres are constrained to slide peak-over-peak, roller boundary conditions are imposed normal to this vertically cut plane for both spheres nullifying normal displacements. Also, an assumption is made, and later confirmed, that under the interferences considered here there is insignificant stress or deformation in areas far from the contact region (half-space assumption). This assumption is reasonable if one considers the fact that the contact radius is much smaller than the radius of the sphere and as such, the stress distribution near the contact region cannot be strongly influenced by the conditions in the bulk of the material. This is also in agreement with the fact that deformations decay as $1/r$, where r is the distance from contact [25], and is compliant with Saint Venant's principle. To take advantage of this each sphere is also cut in half in the horizontal plane. A roller boundary condition is imposed along the top surface of the top hemisphere and the bottom surface of the bottom hemisphere is completely constrained. The end result is the hemisphere model shown in Figure 2(a).

In order to capture the deformations and stresses in the region near the contact, the mesh refinement scheme shown in Figure 2(b) is used. This high level of refinement yielded meshes with many elements. Each hemisphere consists of from about 20,000 to 50,000 elements, depending on the applied interference. As interference increases a finer mesh is generated in a larger volume near contact because higher stresses develop deeper into the hemispheres. Depending on the interference and with that many nodes and elements each simulation in this study takes from 2 days to over a week on a workstation computer with 8 GB of physical memory and a 2.6 GHz dual-core processor.

As discussed earlier, the total sliding distance is broken into n equal steps. This is done in order monitor the phenomena of interest as sliding progresses as well as to help convergence. Generally, the cases in this analysis are run with 40 equal load steps (n=40) with 4 steps added at the end to ensure disengagement (m=4). However, for the higher interference steel-on-steel cases as many as 120 load steps are also used. This is a trial-and-error process as the code will run, usually to just before or after the hemispheres are vertically aligned then a load step will fail to converge. The code can then be restarted at the last successful increment and continued with a smaller load step sizing.

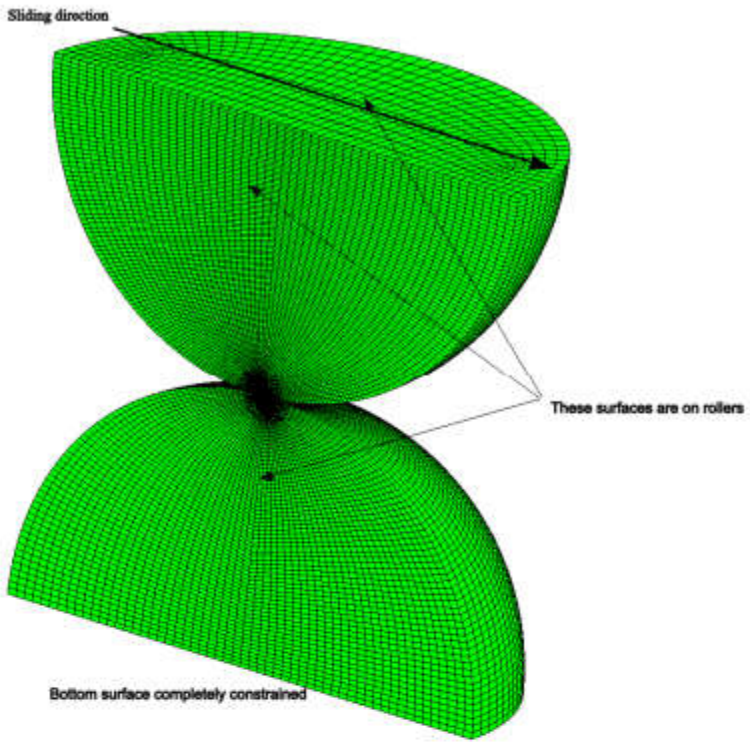

(a)

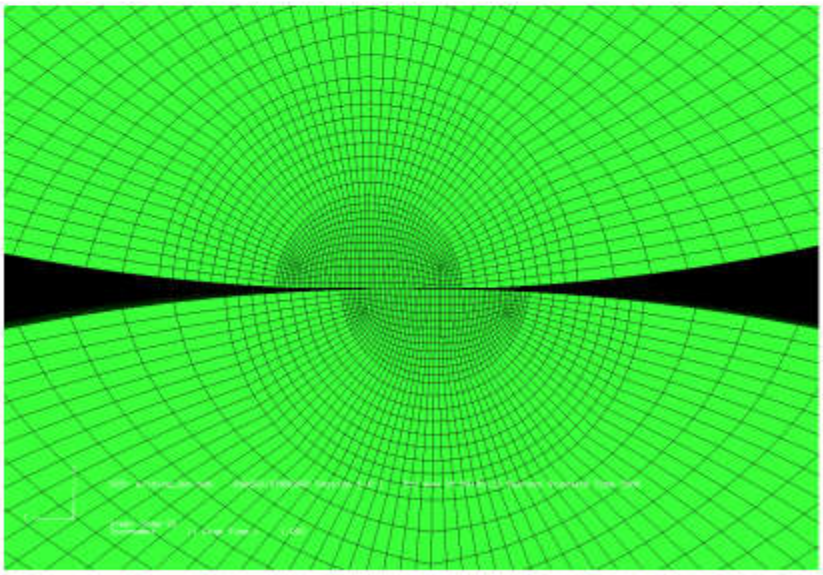

(b)

Figure 2: (a) Model geometry indicating the boundary conditions and sliding direction (b) a zoomed view of the contact region showing the mesh refinement

2.2 Mesh Convergence

The mesh is verified first for a vertically aligned normal elastic contact (non-sliding) with the properties for steel from Table 1 and results are compared against the analytical solution obtained by Green [22]. The FE model is then run past the elastic limit and the results are compared to those in Jackson and Green [26]. For this verification, a downward displacement, ω, is applied to the top hemisphere and the load, P, is monitored. Table 4 presents the normalized load, $P^*=P/P_c$, for the JG model [25] and the current FEA, and the percent errors at a given downward normalized displacement, $\omega^* =\omega/\omega_c$ (critical values are calculated by Eq. (1)). As shown in Table 4, the theoretical and FEA values agree very well with maximum percent errors of 3.2% in the elastic (Hertzian) regime, and 1.6% for the elastic-plastic regime, respectively.

Table 4: Verification of the meshing scheme employed

ω^*	P^* Model	P^* FEA	% Error
0.2	0.089	0.087	-2.7
0.6	0.465	0.450	-3.2
1	1.000	0.989	-1.1
1.4	1.657	1.635	-1.3
1.8	2.415	2.377	-1.6
2.2	3.223	3.180	-1.3
2.6	4.075	4.012	-1.6
3	4.978	4.923	-1.1

Quadrilateral-faced and triangular-faced element meshes are compared. It is found that the quadrilateral-faced elements yields better results with a coarser mesh and are therefore used in order to reduce run time. Additionally, the results are later compared to a semi-analytical method (SAM), also serving to verify the mesh. The FEA

and SAM results compare very well under the conditions they are supposed to, as the detailed comparison shall reveal.

Finally, results for frictionless steel-on-steel sliding contact with an interference equal to the critical interference are compared to the normal loading results presented above. The percent difference is 2.3% between the model results for normal loading at the critical interference [25] and the sliding results herein when the hemispheres are vertically aligned. These two situations must theoretically be equivalent. This, coupled with the fact that the results for the sliding case are perfectly symmetric in the elastic regime, also suggest the results can be given in confidence.

3. Results

3.1. Stresses

As part of this analysis, the stress profile throughout the progression of frictionless sliding is monitored. Figures 3 and 4 present the von Mises stress in the two hemispheres at the point of vertical alignment ($x/R = 0$) for preset vertical interferences of $2\omega_c$ and $15\omega_c$ for steel-on-steel and aluminum-on-copper sliding, respectively. The results are smooth and symmetric about the contact plane for the steel-on-steel case, as expected. In order to show the stress pattern with adequate detail, each image is a close-up of the area near contact. It can be seen, based on the curvature, that the stressed volume penetrates deeper into the hemisphere for the $15\omega_c$ case while maximum values appear at the contact surface (see Figures 3(b) and 4(b)). For the $2\omega_c$ case, the hemispheres have deformed plastically, i.e., the stresses have surpassed their respective yield strength, yet the yielded regions still lie below the surface (see Figures 3(a) and 4(a)). The results are consistent with those reported in [16, 25]. In the aluminum-on-copper sliding with an interference of $15\omega_c$ both hemispheres show a large volume with more significant plastic regions compared to the steel-on-steel sliding case. And because copper is much stiffer and stronger than aluminum (see Table 1) it can sustain higher von Mises stresses. Note that for the $2\omega_c$ cases the maximum von Mises stress is below the surface, while for the $15\omega_c$ case that stress reaches the surface, which is consistent with the findings in [25]. It can be seen in Figures 3 and 4 that the stress values are slightly above the yield strength. This is due to the strain hardening implemented in this analysis. As stated previously, a bi-linear strain hardening of 2% of the elastic modulus is added to the material definition in order to improve convergence.

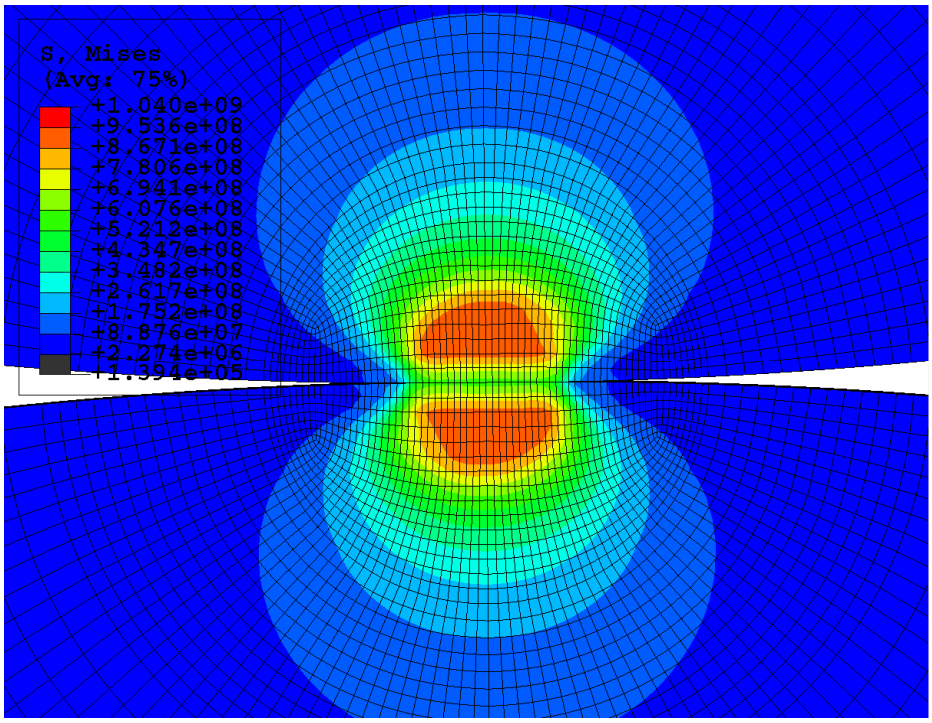

(a)

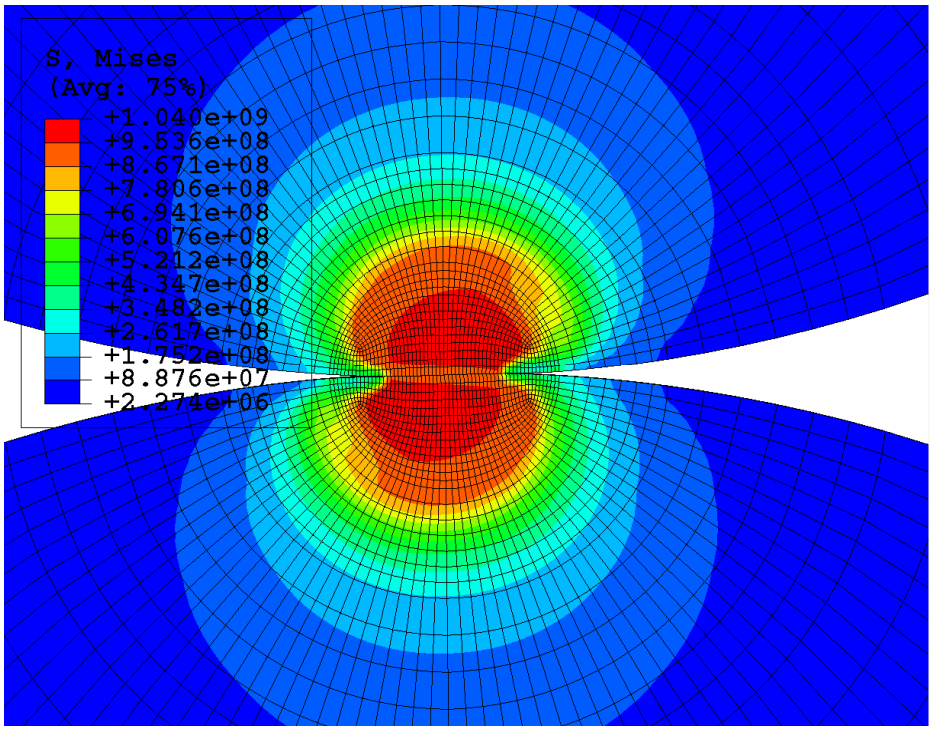

(b)

Figure 3: Von Mises stresses at the point of vertical alignment for steel-on-steel contact for (a) $2\omega_c$ and (b) $15\omega_c$.

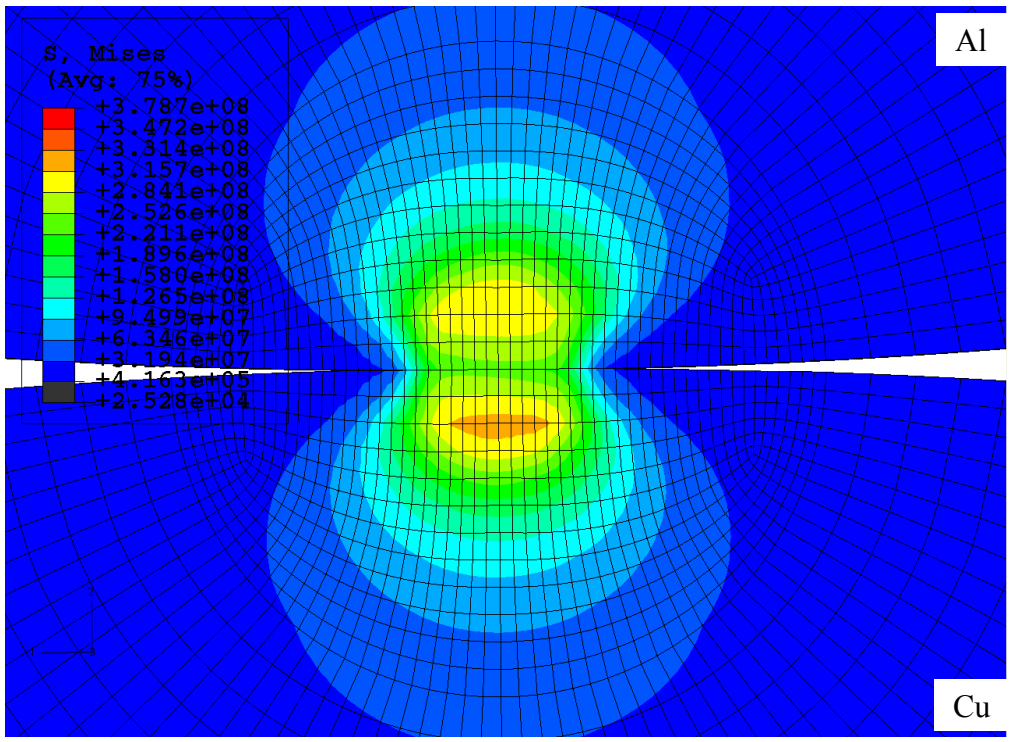

(a)

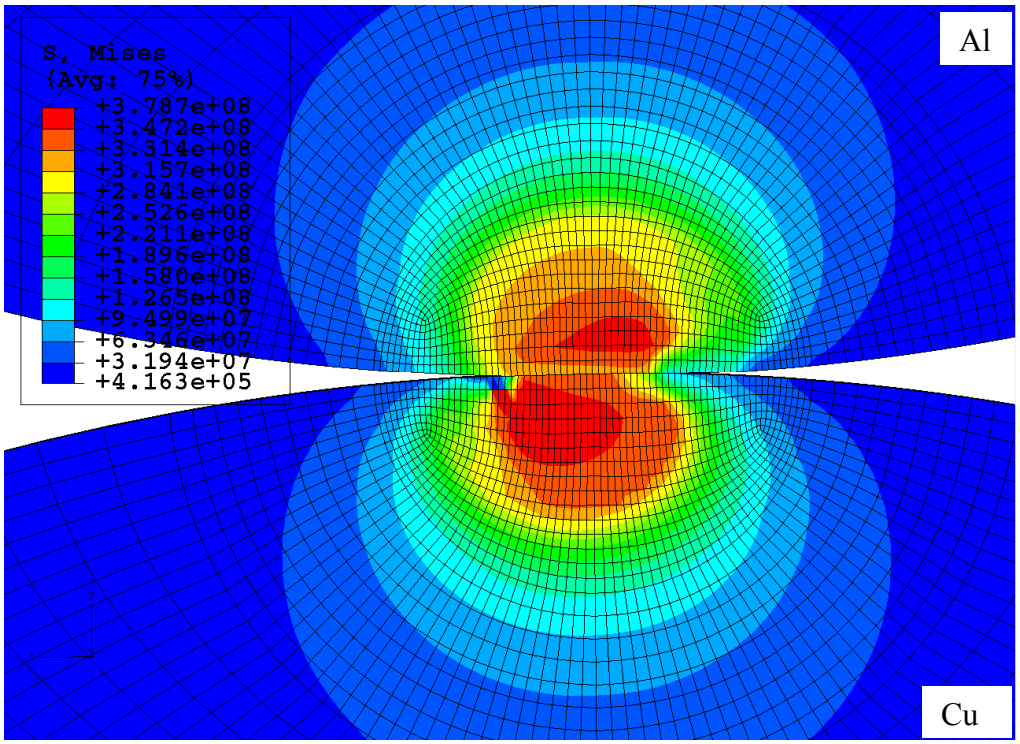

(b)

Figure 4: Von Mises stresses at the point of vertical alignment for aluminum-on-copper contact for (a) $2\omega_c$ and (b) $15\omega_c$.

As sliding progresses the stresses reach peak values occurring near the point of vertical alignment, as shown in Figures 3 and 4. Then the stress magnitude decreases as the hemispheres move away from each other. Figures 5 and 6 present the residual von Mises stresses in the hemispheres once they have come out of contact for steel-on-steel and aluminum-on-copper sliding, respectively. For the $2\omega_c$ cases shown in Figures 5(a) and 6(a), the residual stresses reduced well below the yield strength indicating elastic shakedown, i.e., the stresses have relaxed and the hemispheres would be able to carry more load before yielding again. On the other hand, for the $15\omega_c$ steel-on-steel case, shown in Figure 5(b), the maximum residual stresses are very close to the yield strength. As shown in the figure, the maximum residual von Mises stress is shown to be 911.1 MPa and displays a 0.04% difference to the defined yield strength of 911.5 MPa, which is an insignificant difference. It is interesting to note that for the higher interference case, $15\omega_c$, the highest residual stress regions are at the surface while in the lower interference case, $2\omega_c$, the region of highest residual stresses are still below the surface. In the beginning of the sliding process, the hemispheres first yield plastically below the surface, but as sliding progresses the plastic region expands and eventually reaches the surface. One might expect the highest residual stresses to be in the region where the hemisphere first yielded plastically, but as shown by comparing Figures 3 and 5, this is not the case. These residual stresses could be important if one considers shakedown, which upon successive reloading, the material is subjected to the combined loading of the contact stresses as well as the residual stresses. These residual stresses are protective because they make yielding less likely to occur on subsequent passes [25] should they occur.

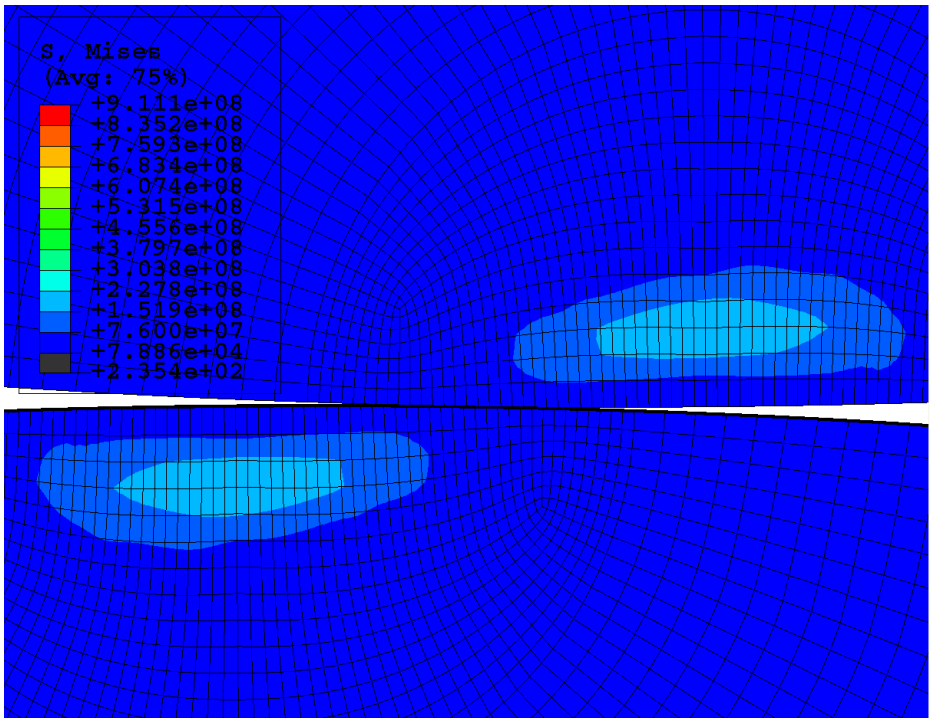

(a)

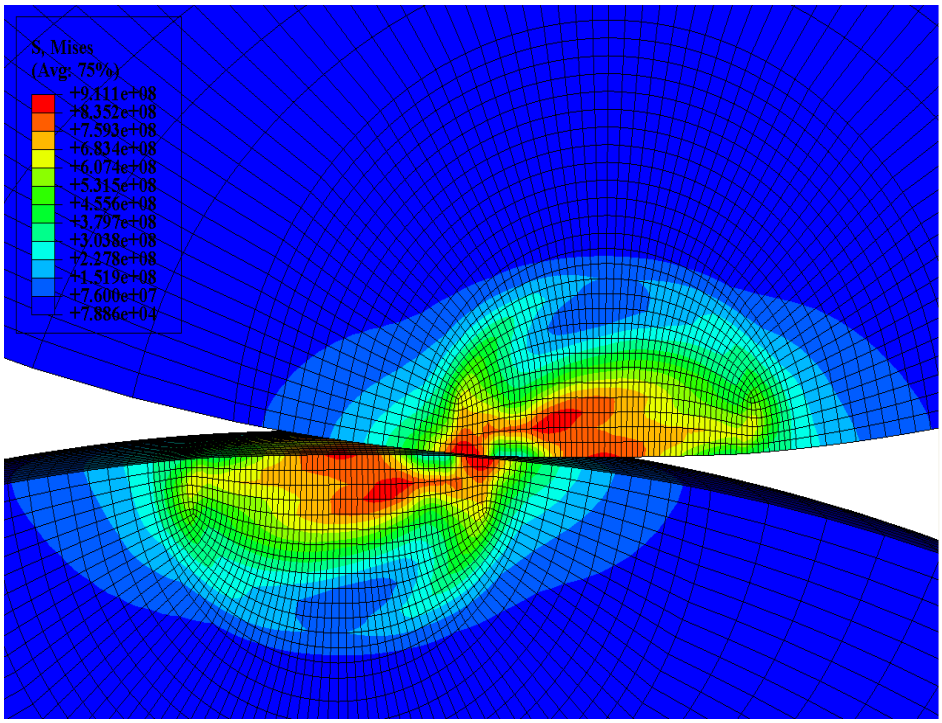

(b)

Figure 5: Residual von Mises stresses at the completion of sliding for steel-on-steel contact for (a) $2\omega_c$ and (b) $15\omega_c$.

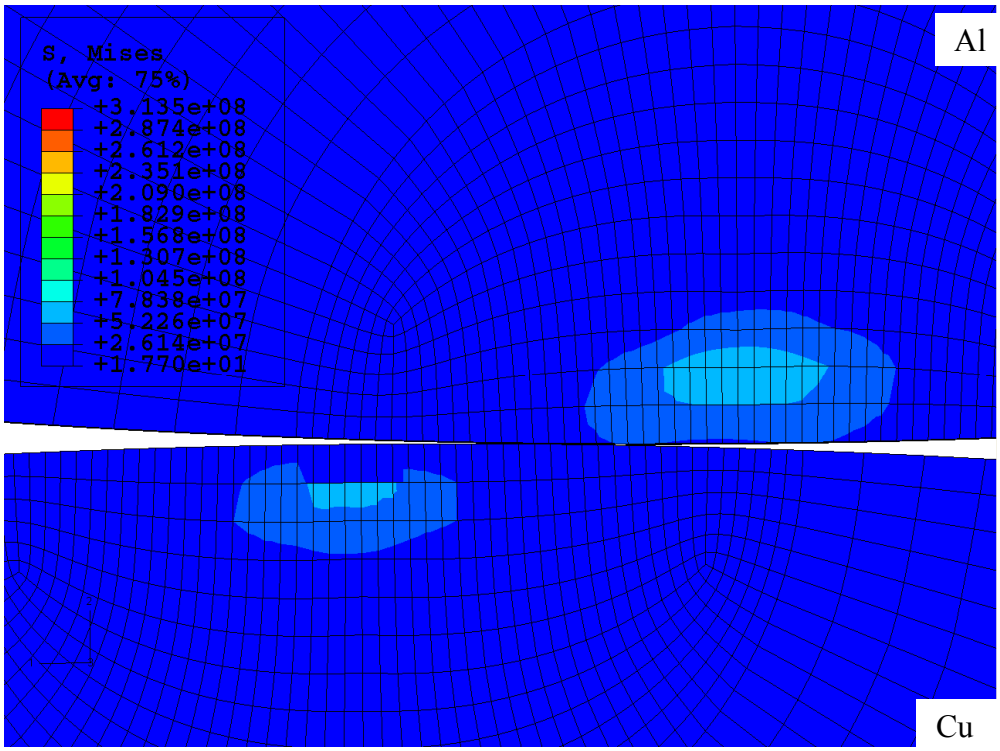

(a)

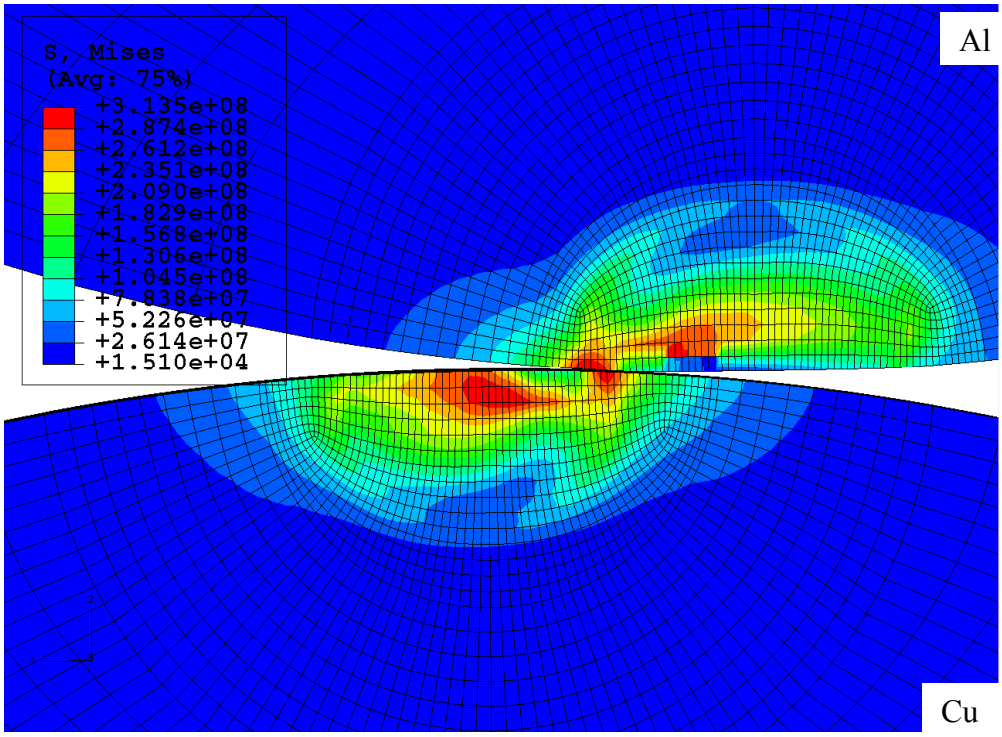

(b)

Figure 6: Residual von Mises stresses at the completion of sliding for aluminum-on-copper contact for (a) $2\omega_c$ and (b) $15\omega_c$.

It is interesting to compare the residual plastic strains in the hemispheres for the material combinations in this analysis. Figures 7 and 8 present the residual plastic strains for steel-on-steel and aluminum-on-copper sliding contact, respectively. As shown in Figure 7, the residual plastic strains are identical in each hemisphere. This is expected as they are identical materials. The lower interference cases, as Figure 7(a) is representative, are nearly symmetric about the center line of the hemispheres and below the surface. As the interference increases, plastic strains reach the surface and the maximum value shifts toward the trailing edge of contact as material is displaced (tugged) in that direction.

Figure 8 displays the residual plastic strains for aluminum-on-copper sliding contact. As shown in the figure, there is significantly more plastic residual strain in the aluminum hemisphere as it is the weaker material (see Table 1). Similar to the steel-on-steel cases, as interference increases, the residual plastic strains become less symmetric and shift toward the contact interface.

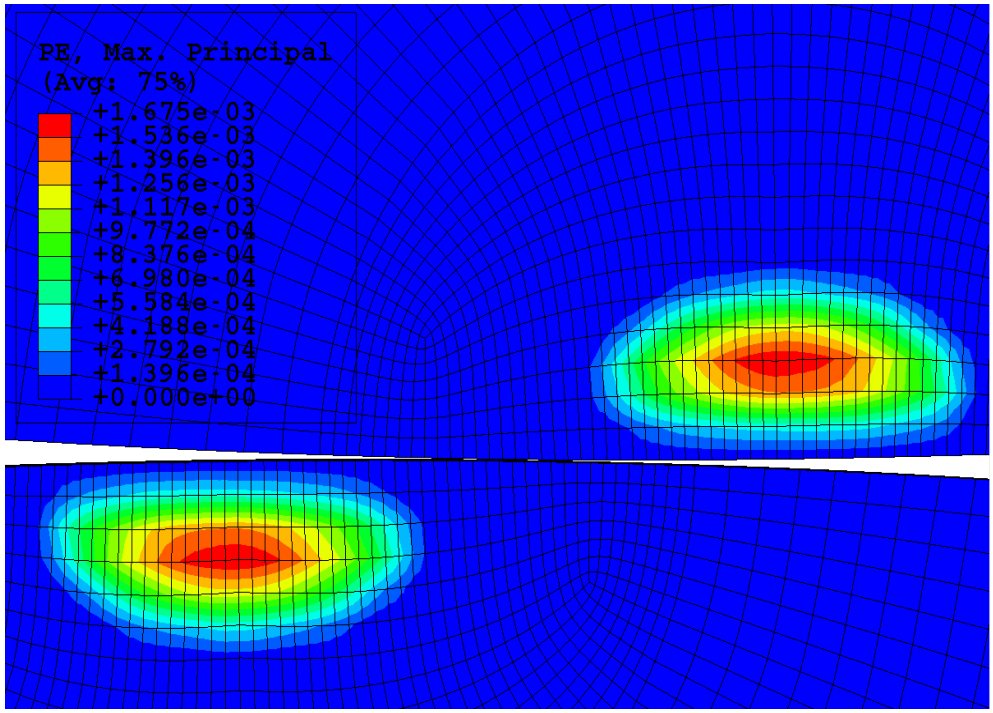

(a)

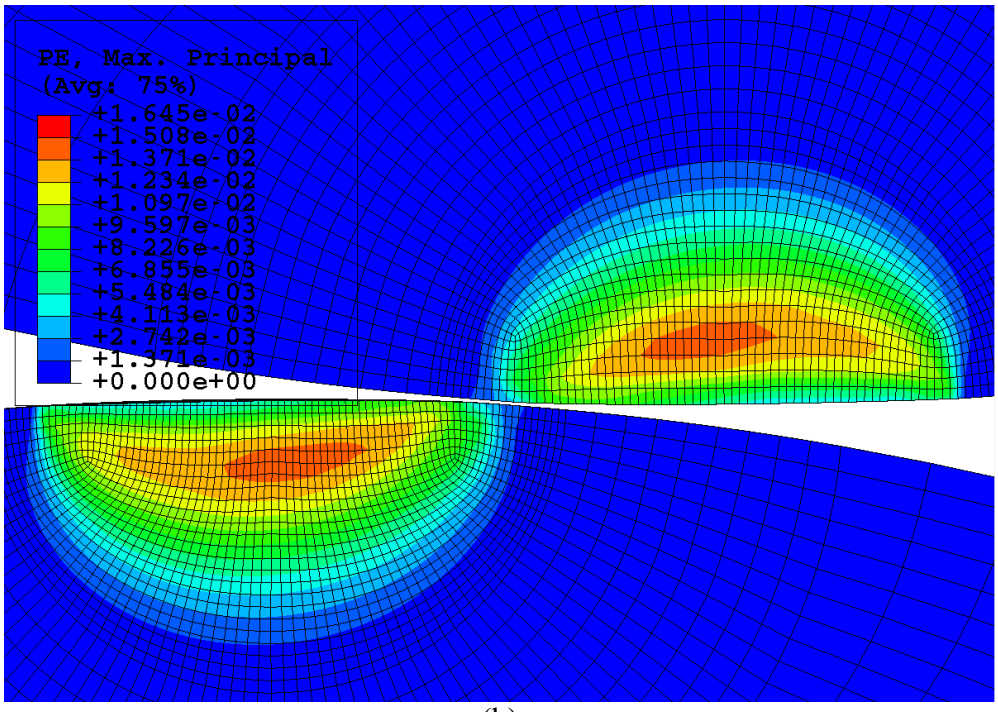

(b)

Figure 7: Residual plastic strains at the completion of sliding for steel-on-steel contact for (a) $2\omega_c$ and (b) $15\omega_c$.

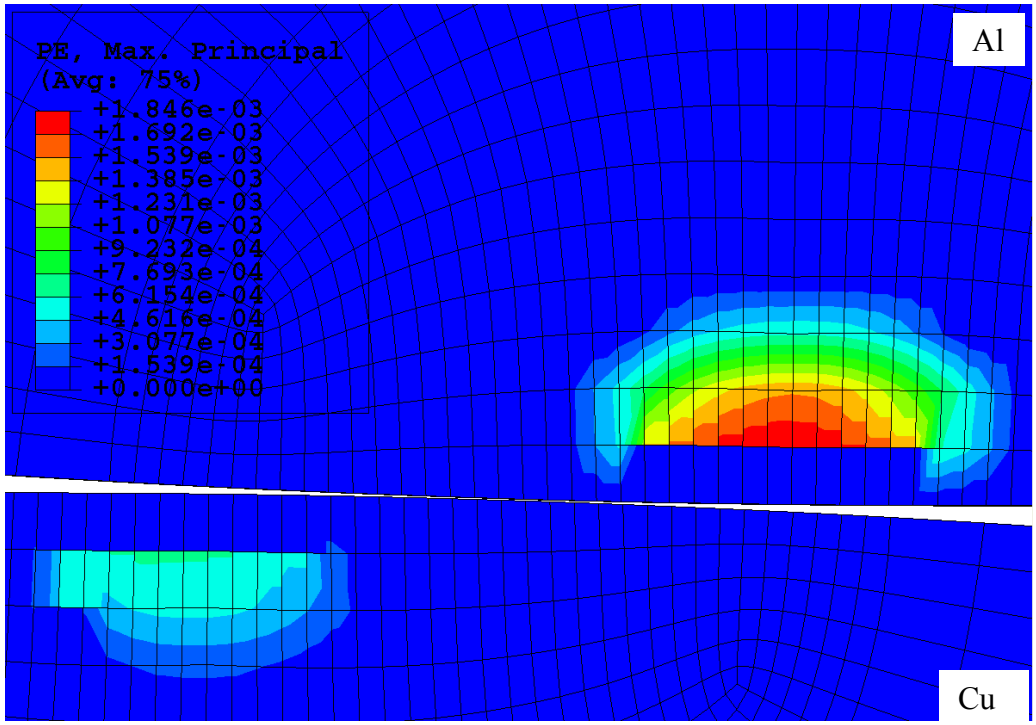

(a)

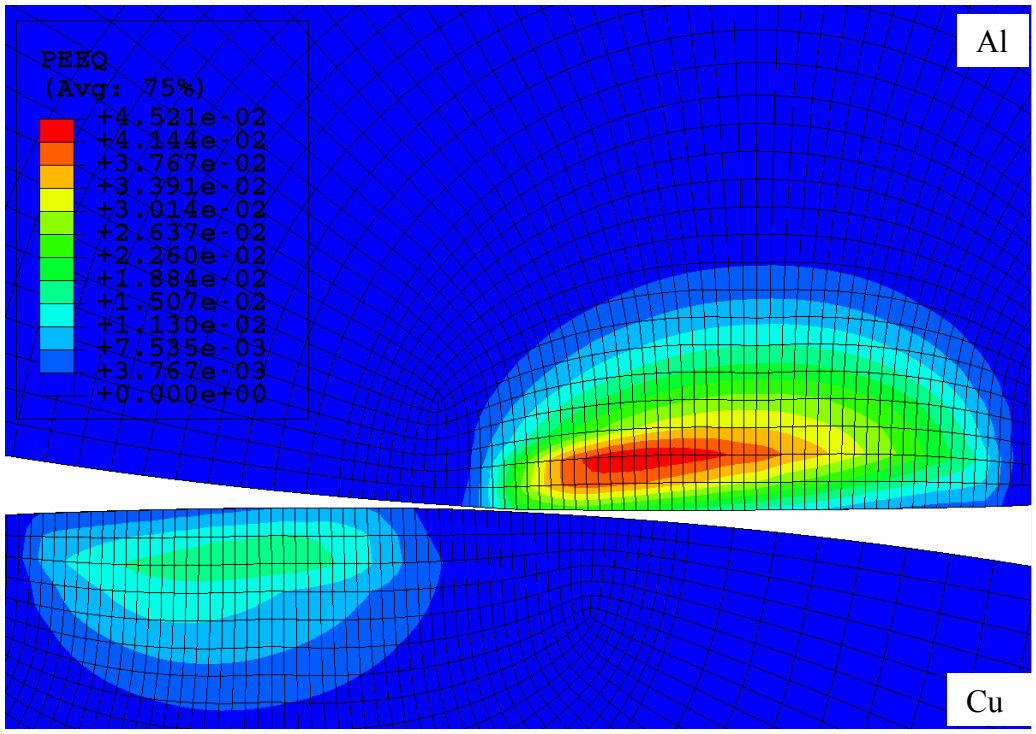

(b)

Figure 8: Residual plastic strains at the completion of sliding for aluminum-on-copper contact for (a) $2\omega_c$ and (b) $15\omega_c$.

Figure 9 presents an oblique view of the von Mises stresses with the upper hemisphere removed at various points in the progression of sliding for a representative and intermediate case of steel-on-steel sliding ($6\omega_c$). The lighter regions in the top of the figures are the top of the hemisphere where contact occurs and the darker regions along the bottom of the figures are the vertically cut face as shown in Figures 3 through 6. This is presented to better visualize how the stress develops along the contacting surface of the hemispheres. Before the hemispheres are vertically aligned, Figure 9(a), a pocket of lower stress surrounded by a high stress ring begins to develop in the contacting region. As sliding progresses further, Figures 9(b) and 9(c), this pocket of lower stress diminishes and a yielded core propagates along the surface where the hemispheres are in contact. Past vertical alignment, Figures 9(c) and 9(d), a pocket of very low stress develops near the high stress core which trails the contact. This low stress pocket continually expands as the hemispheres come out of contact. Figure 9(d) presents the residual stress in the hemisphere with a much expanded low stress pocket.

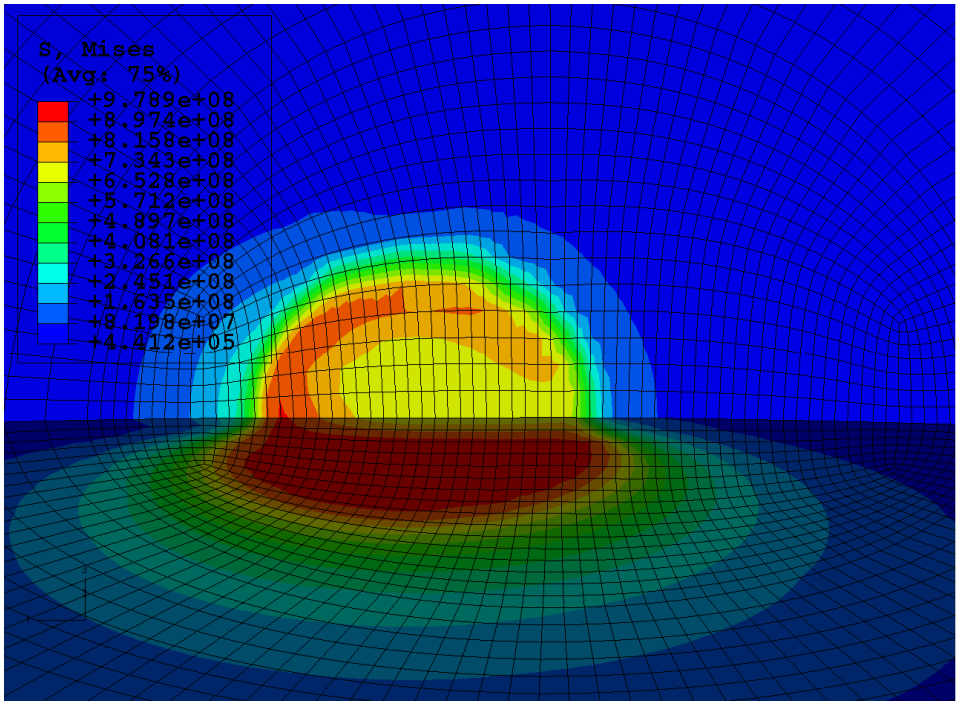

(a)

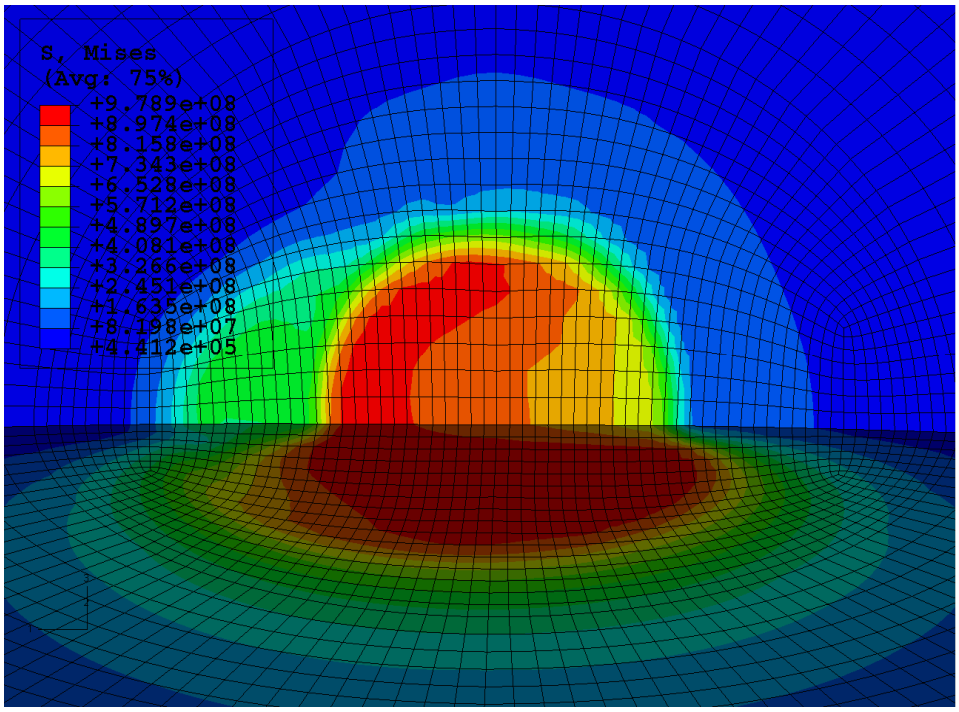

(b)

Figure 9: An oblique view of the von Mises stress in one hemisphere for steel-on-steel contact at an interference of $6\omega_c$ at (a) one-fourth and (b) half of the sliding distance.

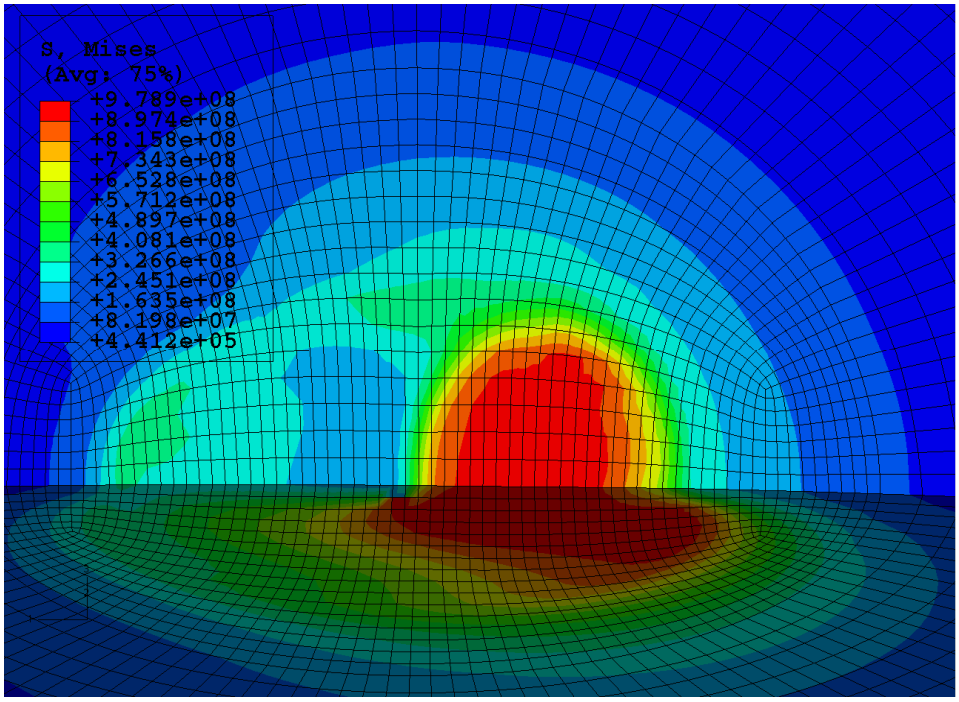

(c)

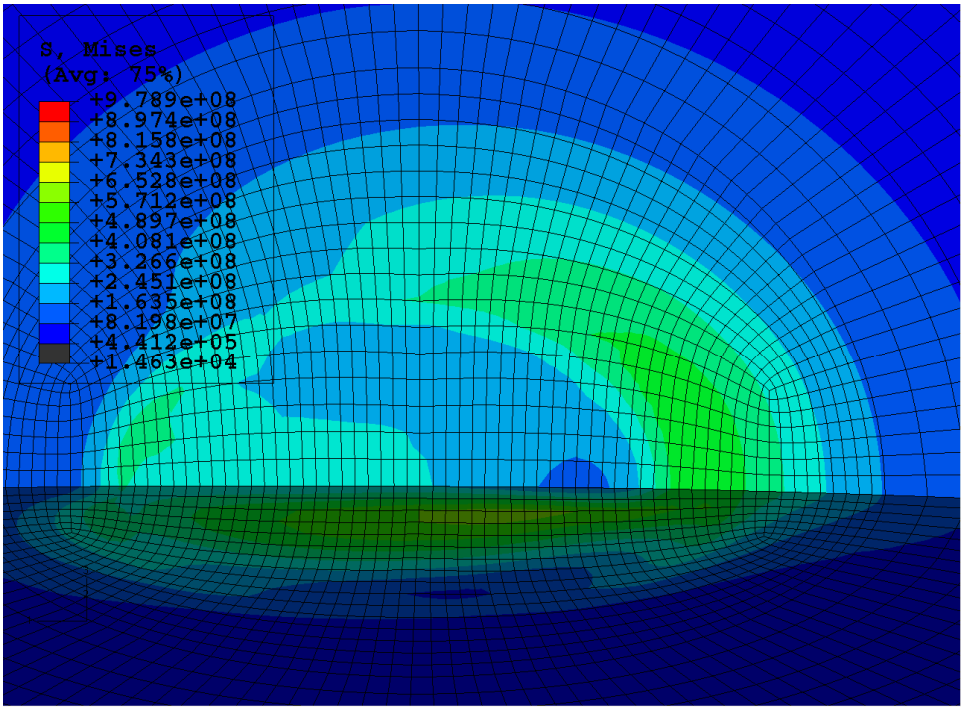

(d)

Figure 9 continued: An oblique view of the von Mises stress in one hemisphere for steel-on-steel contact at an interference of $6\omega_c$ at (c) three fourths and (d) the completion of the sliding distance.

3.2. Forces

The reaction forces on the bottom hemisphere as sliding progresses are also monitored in this study. The action-reaction principle indicates that the reaction forces on the top hemisphere should be identical to that on the bottom hemisphere but in the opposite direction in order to maintain equilibrium. As such, the reaction forces at the base nodes of the bottom hemisphere are summed for each load step and plotted against the normalized horizontal sliding distance, x/R. Figures 10 and 11 present the normalized horizontal reaction forces, F_x/P_c, for the various preset vertical interferences for steel-on-steel contact, and aluminum-on-copper contact, respectively. The normalized vertical reaction forces, F_y/P_c, for steel-on-steel contact, and aluminum-on-copper contact are presented in Figures 12 and 13, respectively. These reaction forces are normalized by the critical load, P_c, as defined previously in Eq. (1).

As sliding begins the horizontal forces start from zero and increase in magnitude to a maximum value then begin to decrease before the hemispheres are vertically aligned ($x/R = 0$). As shown in Figures 10 and 11, the lower interference cases show a nearly anti-symmetric pattern about the x/R axis indicating that very little plastic deformation and, although not shown in the figures, cases run at the critical interference display a perfectly anti-symmetric pattern. As the interference increases, more plastic deformation occurs. This can be seen by the larger magnitude of the negative forces as the hemispheres slide toward vertical alignment compared to the smaller positive force values as the hemispheres come out of contact. As can be seen, the horizontal force is not zero at the point of vertical alignment. This can be attributed to material being

displaced (tugged) in the direction of sliding impeding the sliding progress even after the hemispheres are vertically aligned.

The normalized vertical reaction force, F_y/P_c, as shown in Figures 12 and 13, show a nearly symmetric pattern about the x/R axis (vertical alignment). As interference increases the maximum forces occur earlier in the sliding progression. This can be attributed to the fact that plasticity is initiated earlier as interference increases. As the material model is nearly elastic-perfectly plastic there is little increase in load carrying capacity in the yielded portion of the hemisphere due to the plastic region just expanding, or flowing under increased load. It can be seen, when comparing Figures 12 and 13, that the curves are nearly identical on a case-by-case basis. This implies that the vertical reaction force, F_y, is normalized well by the critical load, P_c for both steel-on-steel and aluminum-on-copper contact.

It should also be noted, by comparing Figures 12 and 13, how well P_c normalized the reaction force. For instance, if one compares the maximum normalized vertical reaction force of both material combinations for the same normalized vertical interference, they are nearly identical.

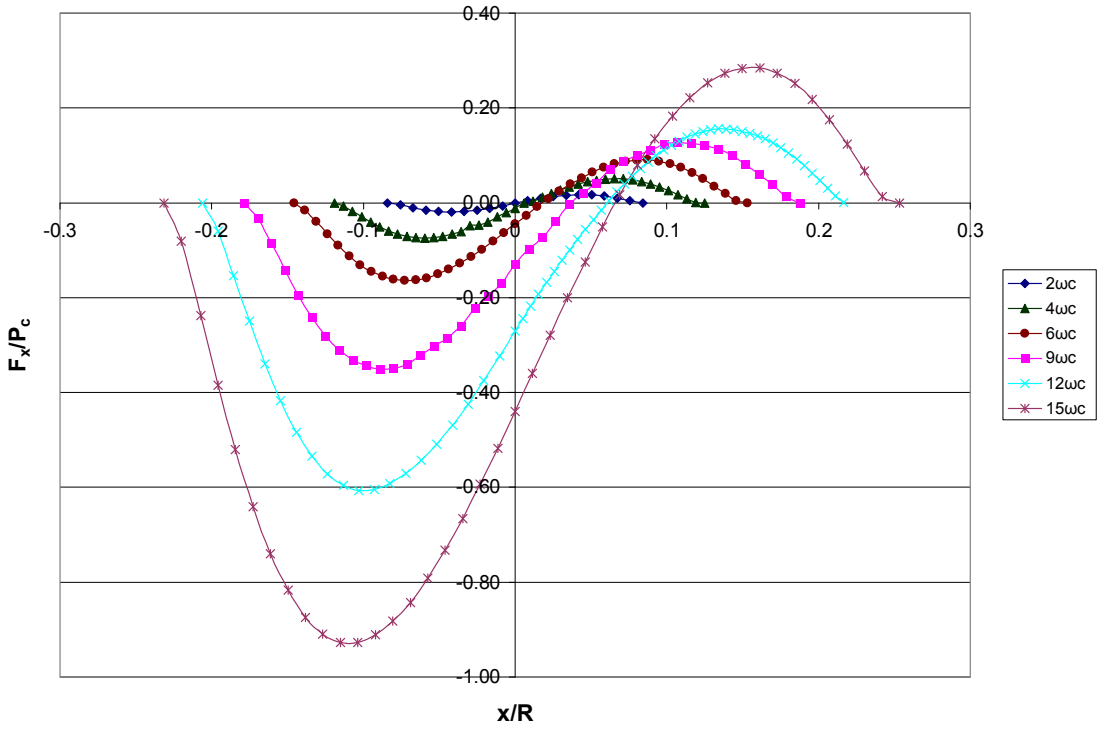

Figure 10: Normalized horizontal reaction forces for $2\omega_c$ through $15\omega_c$ for steel-on-steel contact.

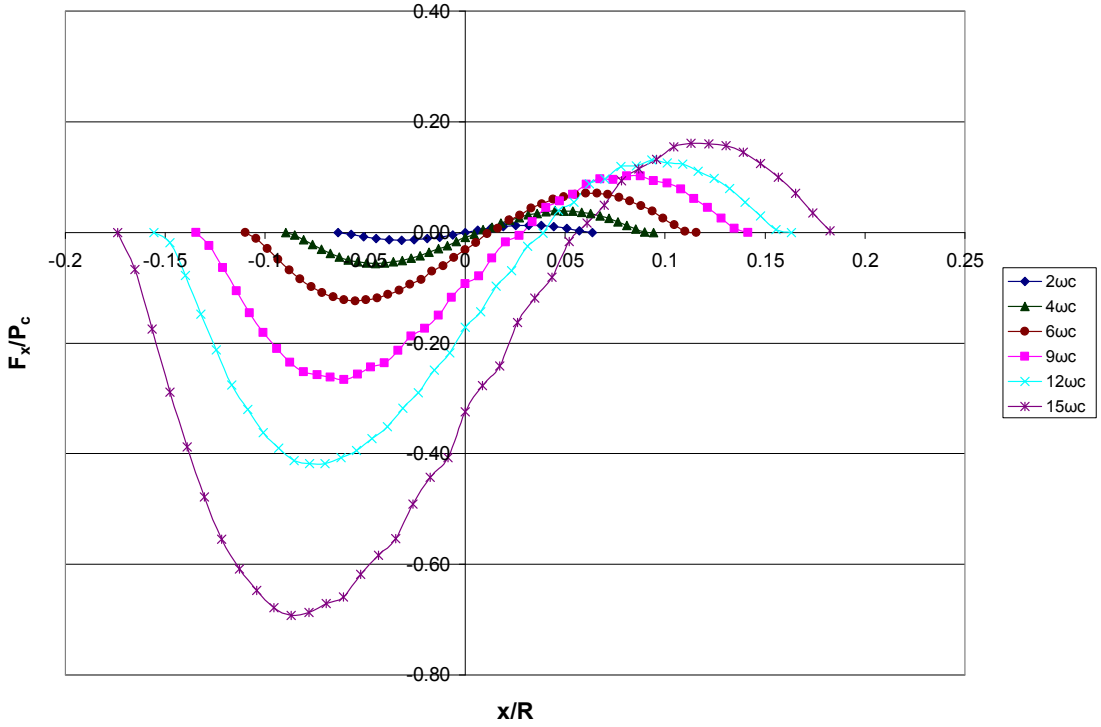

Figure 11: Normalized horizontal reaction forces for $2\omega_c$ through $15\omega_c$ for aluminum-on-copper contact.

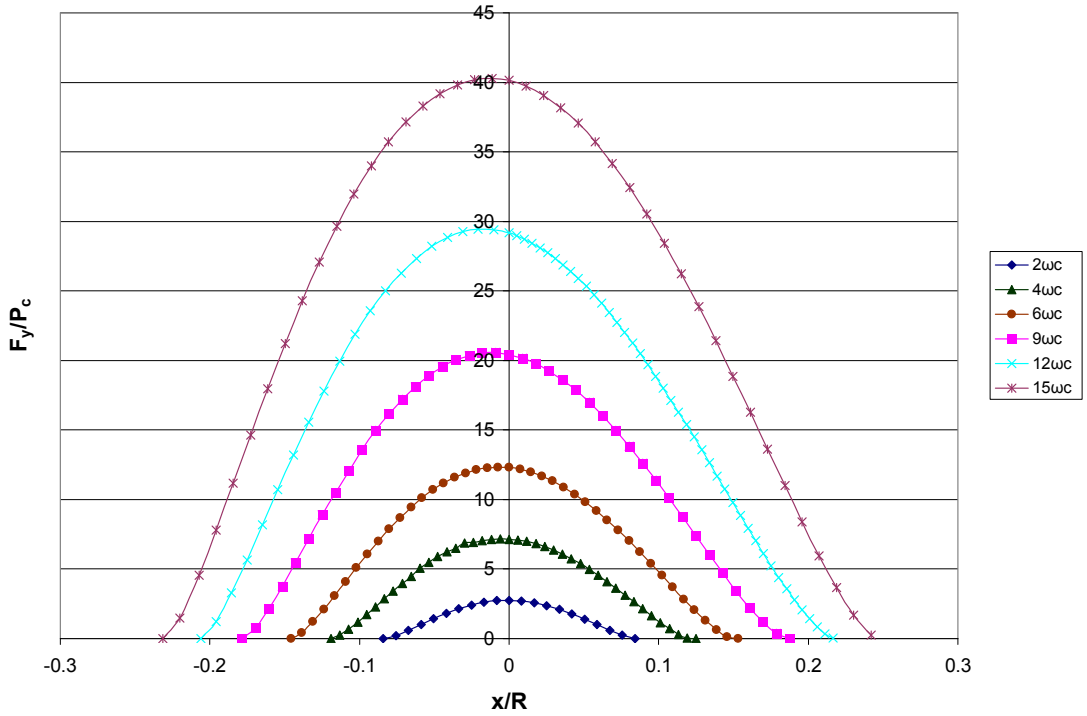

Figure 12: Normalized vertical reaction forces for $2\omega_c$ through $15\omega_c$ for steel-on-steel contact.

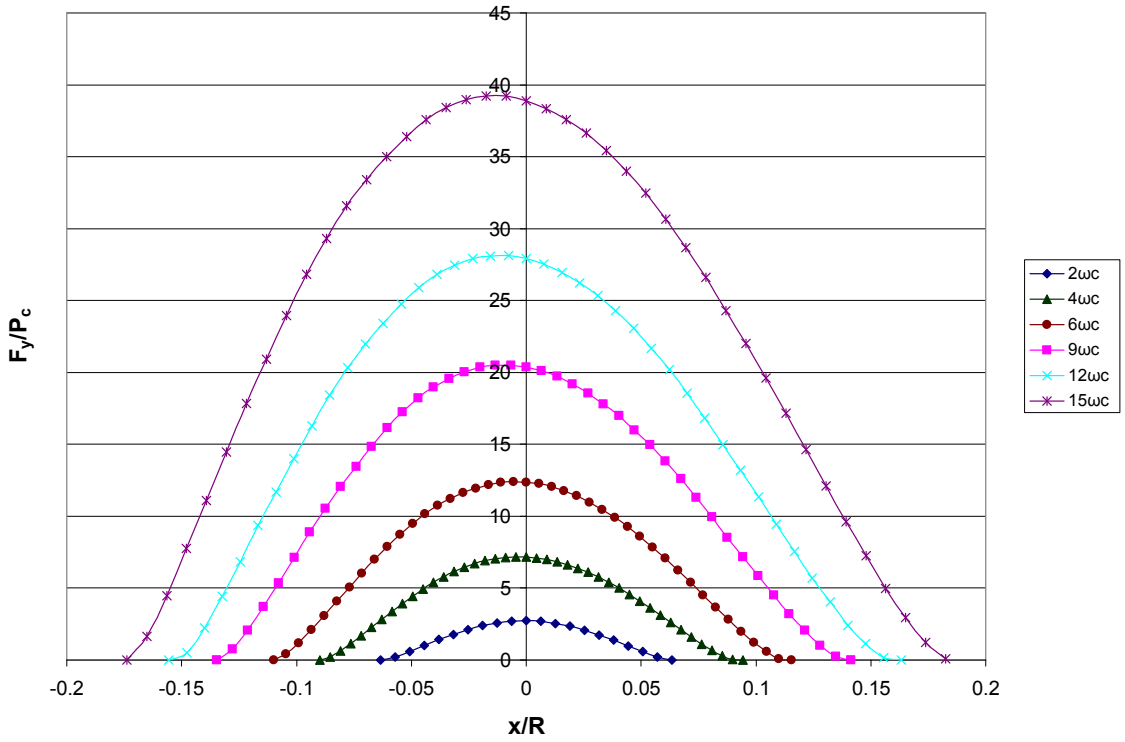

Figure 13: Normalized vertical reaction forces for $2\omega_c$ through $15\omega_c$ for aluminum-on-copper contact.

As there is no friction coefficient imposed in this analysis a “load ratio” is defined as F_x/F_y, being the ratio of the horizontal reaction force over the vertical reaction force in order to better understand the resistance to sliding due to the mechanical interference. While each of the data points on these curves can be thought of as qualitatively similar to the instantaneous local coefficient of friction, it is emphasized that this is not a coefficient of friction in the traditional sense since other effects (e.g., adhesion, surface contamination) are not accounted for. Moreover, in the region where the hemispheres repel each other, the positive “load ratio” should not be interpreted as a negative coefficient of friction. This ratio is generated and plotted versus the normalized sliding distance as shown in Figures 14 and 15 for steel-on-steel and aluminum-on-copper, respectively.

It can be seen that the maximum magnitude of the load ratio increases steadily as the preset vertical interference increases. In addition, the plot clearly shows that for all vertical interferences, the maximum magnitude of the load ratio during loading is always greater than the maximum magnitude during unloading. It is also clear from the plot that the ratio of the horizontal to the vertical reaction force is not zero at the point where the hemispheres are vertically aligned. This is due to material being displaced (tugged) in the direction of sliding further opposing the motion. Also of note is the trend of a sharply increasing load ratio as the hemispheres are coming out of contact that occurs for increasing preset vertical interference cases. This is due to the increasing plastic deformation as interference increases. This increase in plastic deformation results in more flattening of the hemispheres in the region of contact, which subsequently reduces the vertical reaction force required to maintain a straight line contact.

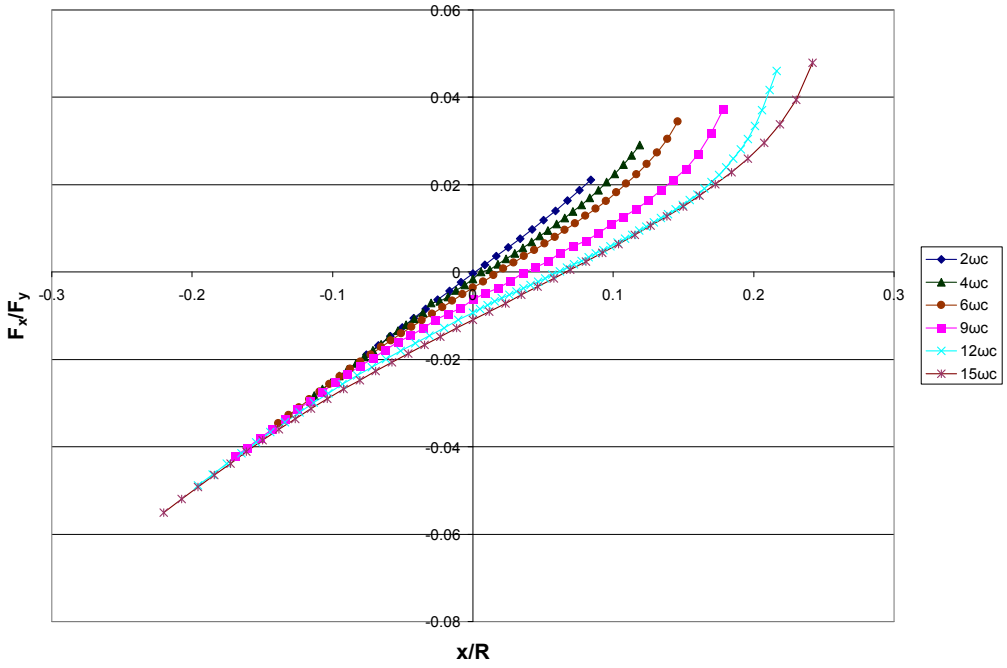

Figure 14: The "load ratio" as sliding progresses for $2\omega_c$ through $15\omega_c$ for steel-on-steel contact.

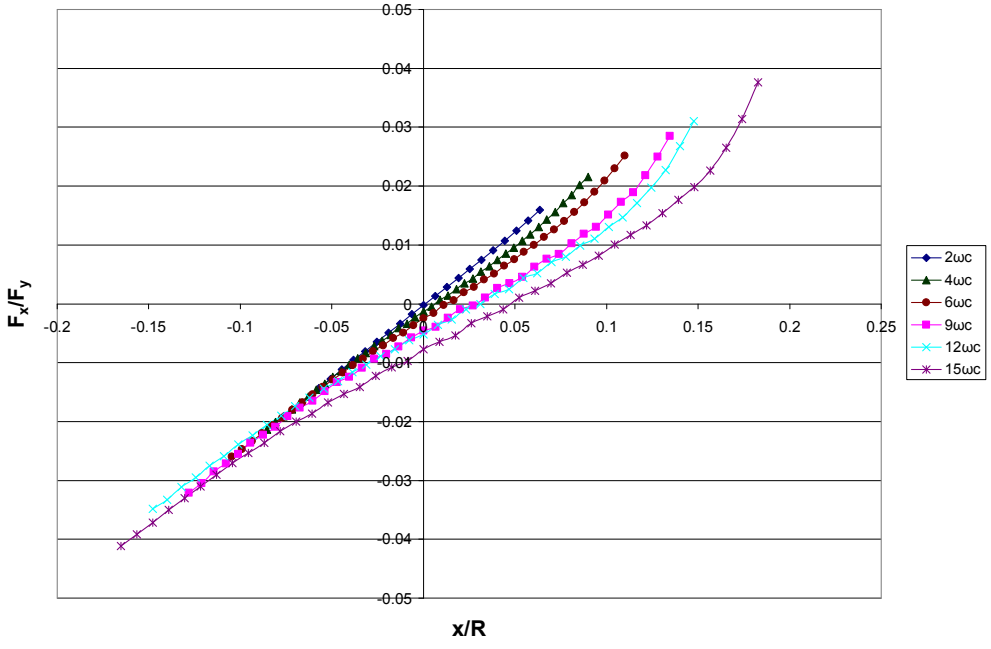

Figure 15: The "load ratio" as sliding progresses for $2\omega_c$ through $15\omega_c$ for aluminum-on-copper contact.

3.3. Energy Loss

Since there is no vertical displacement allowed along the top and bottom boundaries of the hemispheres, the net energy loss in sliding can be defined as

$$U_{net} = \int_{x_1}^{x_2} F_x dx \tag{9}$$

where x_1 and x_2 respectively represent the starting and ending sliding positions of the top hemisphere. This equation is used to quantify the work done when sliding the top hemisphere over the bottom hemisphere. Thus, energy loss in sliding, U_{net}, for individual preset vertical interference cases is essentially the absolute net area under the horizontal reaction curves given in Figures 10 and 11. The net energy loss in sliding for each individual preset vertical interference case is normalized by U_c given by Eq. (8) and the corresponding values in Table 2, and these are plotted against the normalized preset interference, $\omega^* = \omega / \omega_c$. These values are shown in Figure 16 for steel-on-steel and aluminum-on-copper sliding.

For both steel-on-steel and aluminum-on-copper sliding the energy loss increases drastically as the preset interference increases. In a completely elastic case the work invested in sliding the hemispheres into alignment will be equal to the energy restored as the hemispheres slide out of alignment. The work required to slide the hemispheres to vertical alignment can be thought of as a loading effect similar to a spring being compressed. Past the point of vertical alignment the hemispheres repel each other, similar to a spring being restored.

As the preset interference increases, more of the material becomes plastically deformed as sliding progresses. The portions of the hemispheres that are still elastic once

they are past vertical alignment still do work as they are separating. However, this elastic rebound work will be smaller than the work invested to slide to vertical alignment and beyond due to the plastic deformation. These effects can also be seen in horizontal reaction force curves shown in Figures 10 and 11. As the interference increases, the work invested (negative portion of the curve) increases faster than the elastic rebound work (positive portion of the curve) resulting in progressively more net energy loss.

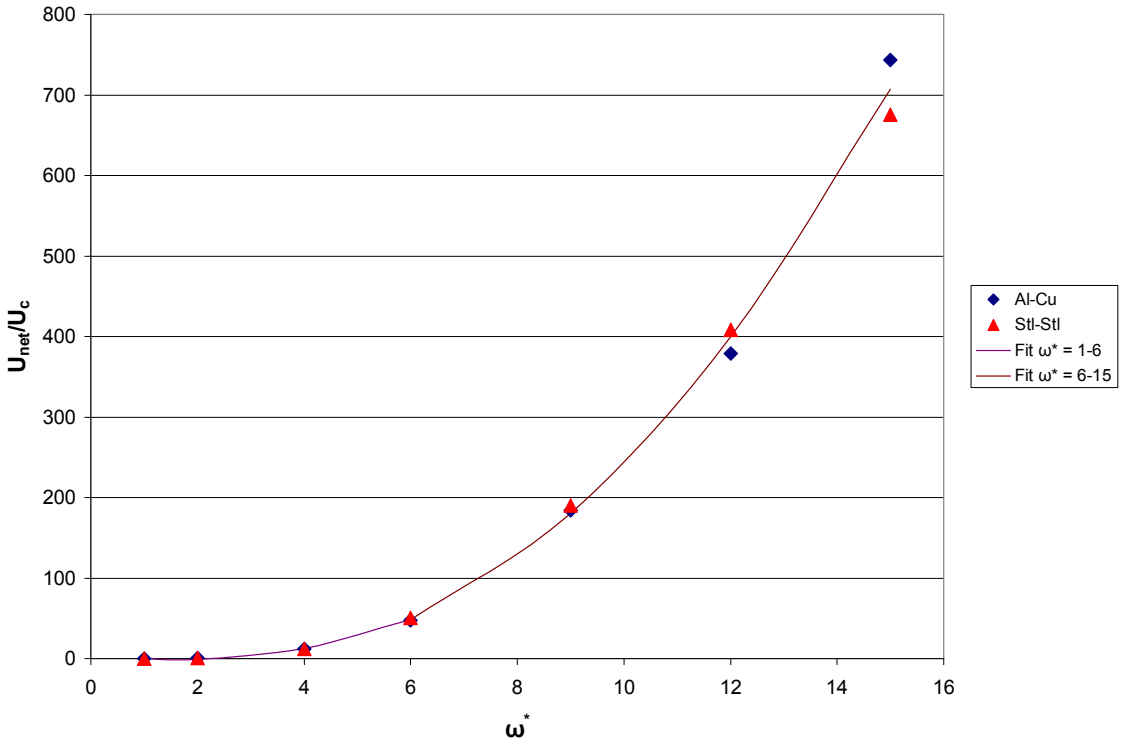

Figure 16: Normalized net energy loss versus preset normalized interference.

As shown in Figure 16, the results for the normalized net energy loss are very close for both aluminum-on-copper sliding and steel-on-steel sliding at a given vertical interference, indicating that U_c normalizes the two cases well. Therefore, a single

exponential curve is fitted to the numerical data of both cases. It represents the trend followed by the energy loss for different ranges of the applied interference, ω^*. Very closely it captures the increasing energy loss with increasingly elastic-plastic loading. Hence,

$$\frac{U_{net}}{U_c} = 0 \qquad \omega^* \le 1$$
$$\frac{U_{net}}{U_c} = 0.6(\omega^* - 1)^{2.7} \qquad 1 \le \omega^* \le 15 \tag{10}$$

with continuity at $\omega^* = 1$.

3.4. Effective Coefficient of Friction

An effective coefficient of friction, μ_{eff}, is introduced as an alternative way to characterize the net energy loss in sliding. A fundamental model is introduced in Figure 17 to help explain this concept. The figure depicts a block, with a normal force, F_y, acting downwards and being pushed across a flat surface by a force, F_x. It is well known that under the conditions depicted in the figure the force required to slide the block across the surface is given by:

$$F_x = \mu F_y \tag{11}$$

where μ is the coefficient of friction (no distinction is made whether it is a "static" or "kinetic" coefficient of friction). Combining this expression with the definition of work done in sliding results in:

$$W = \int_{x_1}^{x_2} F_x dx = \int_{x_1}^{x_2} \mu F_y dx \tag{12}$$

Upon rearrangement of this equation one can define a new expression for the effective coefficient of friction, μ_{eff} , given by:

$$\mu_{eff} = \frac{W}{\int_{x_1}^{x_2} F_y dx} \tag{13}$$

This μ_{eff} is an effective coefficient of friction for the entire sliding process.

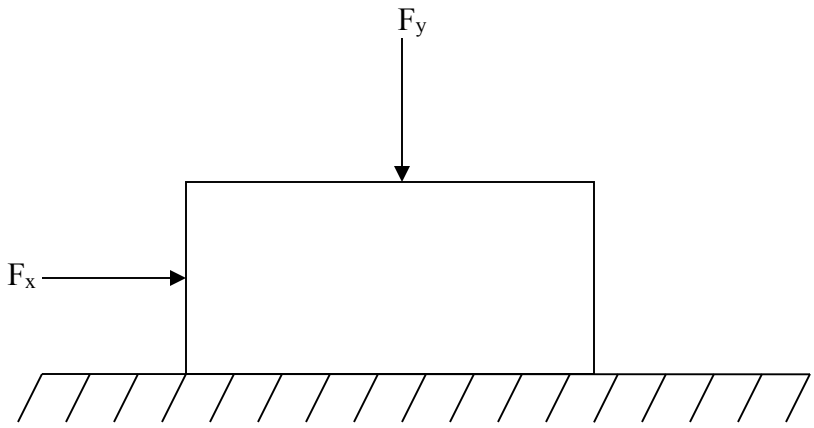

Figure 17: A fundamental schematic of a sliding process.

It has been shown in this analysis that there is resistance to even sliding without an imposed coefficient of friction. This is caused by hemispherical sliding in the presence of a mechanical interference. As such, an effective coefficient of friction can be defined:

$$\mu_{eff} = \frac{U_{net}}{\int_{x_1}^{x_2} F_y dx} \tag{14}$$

where U_{net} is defined in Eq. (9). Figure 18 presents the effective coefficient of friction for the various preset vertical interferences. As shown in the figure, both steel-on-steel and aluminum-on-copper start with $\mu_{eff} = 0$ for $\omega^* \leq 1$, and then μ_{eff} for the two material

combinations begins to diverge with increasing interference. The effective coefficient of friction tends to flatten out slightly as interference increases due to an increasing amount of flattening of the hemispheres, thus reducing the resistance to sliding.

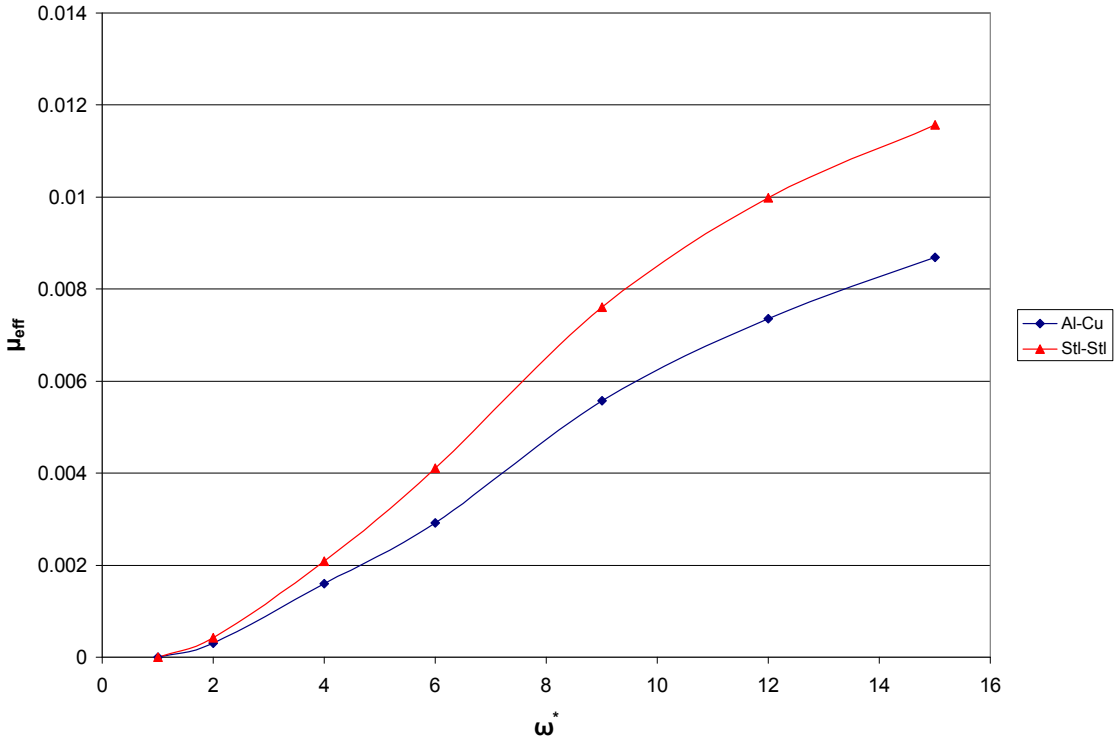

Figure 18: The effective coefficient of friction versus vertical interference.

The effective coefficient of friction in frictionless sliding can be thought of as the contribution of mechanical deformation to the resistance to sliding, or friction coefficient. Since these values are much smaller than friction coefficients measured in practice (by an order of magnitude), it must be concluded that friction as a phenomenon has a strong interfacial component that is not accounted for in this analysis.

3.5. Contact Area

The real contact area throughout sliding is also investigated in this analysis. The real area of contact is important in many instances. For example, electrical and thermal contact resistance is a function of the real area of contact, which changes depending on the loading condition. Figures 19 and 20 present a plot of the normalized contact area, $A^*=A/A_c$ (where A_c is given in Eq. (1)), versus normalized sliding distance, x/R. For small vertical interferences the contact area shows a nearly symmetric pattern. As interference increases, the location of maximum contact area occurs progressively earlier in the progression of sliding, similar to the vertical reaction force as presented in Figures 12 and 13. Also, the aluminum-on-copper contact situation shows a larger normalized contact area than the steel-on-steel contact situation for a given preset vertical interference. It is noted that the contact area snaps down to a smaller value at the point of vertical alignment. That is caused at the transition from material compression and tugging to repulsion and elastic spring-back.

The jaggedness of the contact area curves can be attributed to the resolution of the model. The contact area can only be calculated based on nodal coordinates. The model is composed of discrete elements so even if the contact area extends past the element boundary just slightly, ABAQUS will only recognize the whole element as being in contact. Even with this resolution issue Figures 19 and 20 do present the general trend seen in the contact area for different vertical interferences as sliding progresses for both cases studied.

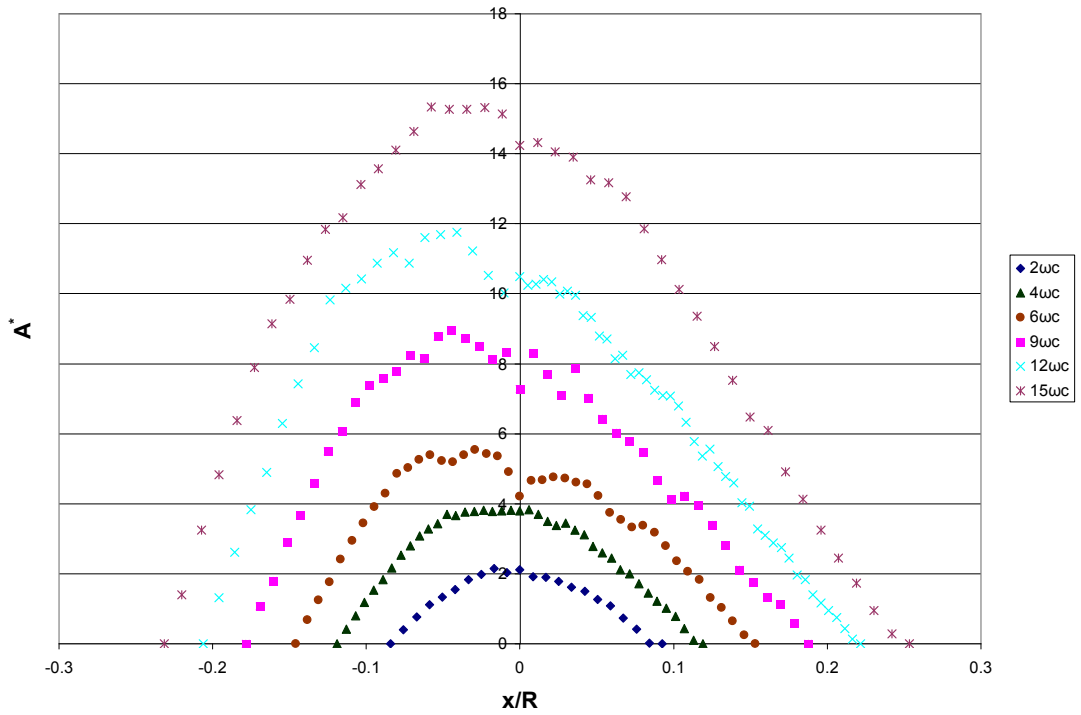

Figure 19: Normalized contact areas for $2\omega_c$ through $15\omega_c$ for steel-on-steel contact.

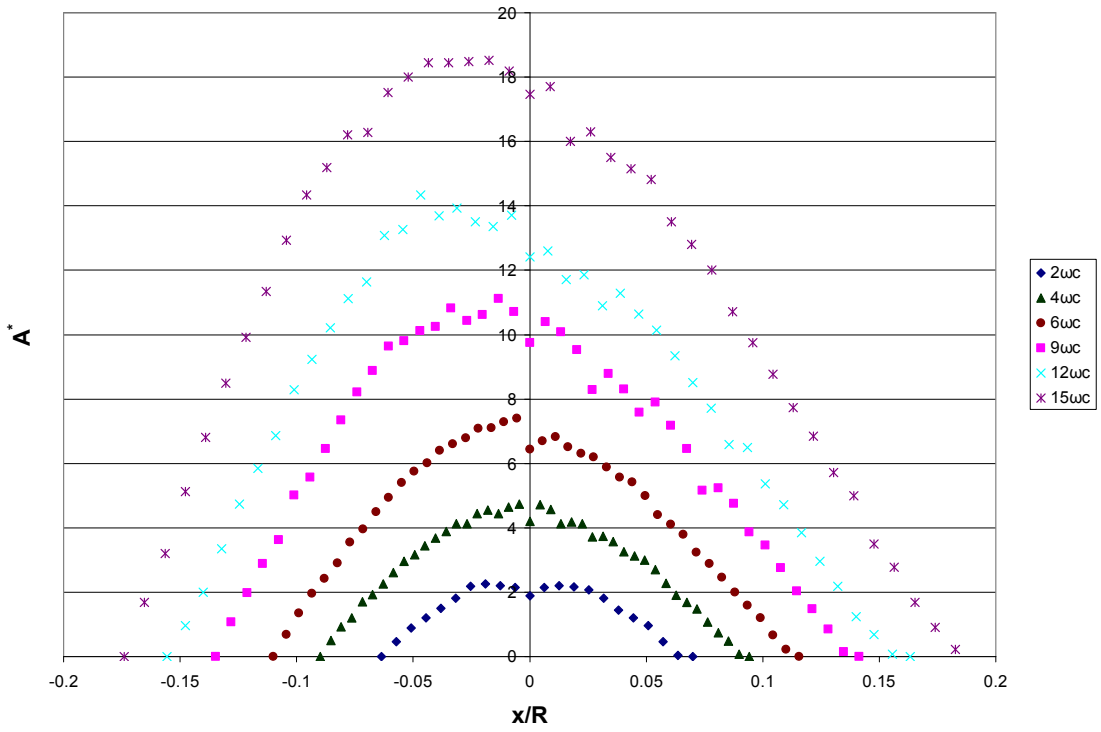

Figure 20: Normalized contact areas for $2\omega_c$ through $15\omega_c$ for aluminum-on-copper contact.

3.6. Deformations

The resulting deformations in the hemispheres as sliding progresses are studied in this analysis as well. Figure 21 presents the maximum normalized vertical deformation, u_{max}/ω_c, in the hemispheres versus normalized sliding distance, x/R, for steel-on-steel contact. As shown in the figure, the deformation increases to a maximum value past the point of vertical alignment and then decreases until the hemispheres come out of contact.

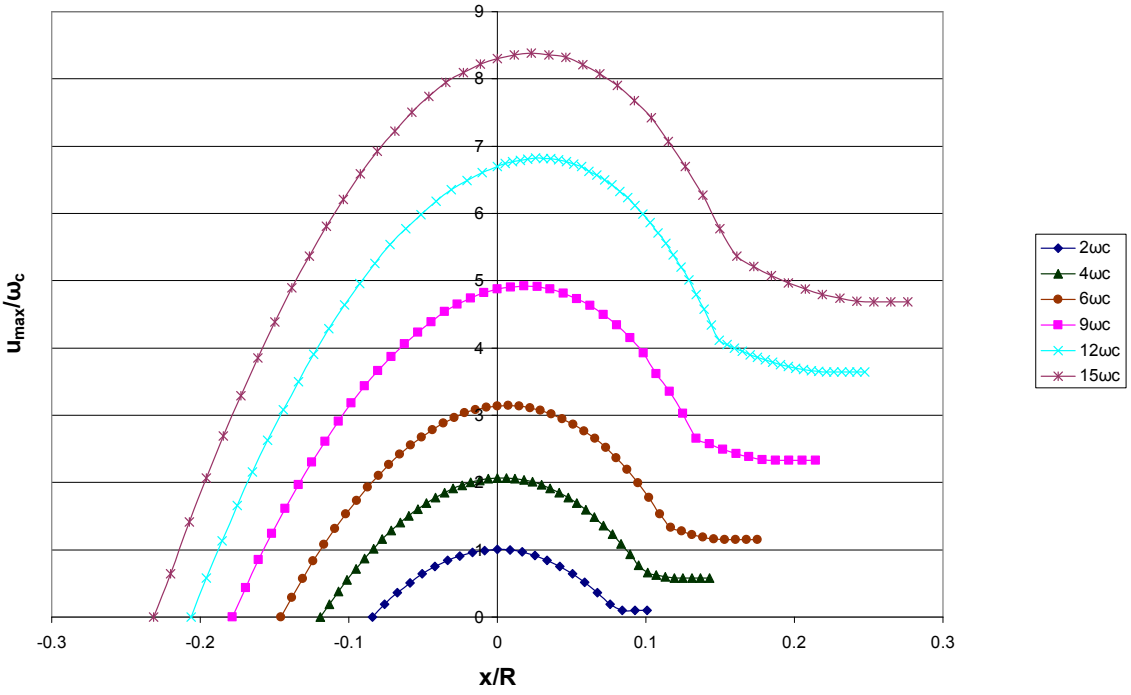

Figure 21: The maximum normalized vertical deformation as a function of sliding position for steel-on-steel contact.

In the aluminum-on-copper contact cases, the materials are different and thus they deform differently. Figures 22 and 23 present the normalized deformation in aluminum and copper, respectively, as sliding progresses for the interferences studied. As shown in the figures, the aluminum deforms much more than the copper due to its much lower

elastic modulus and somewhat lower yield strength (see Table 1). Qualitatively, though they show a similar trend to each other as well as to the steel-on-steel case.

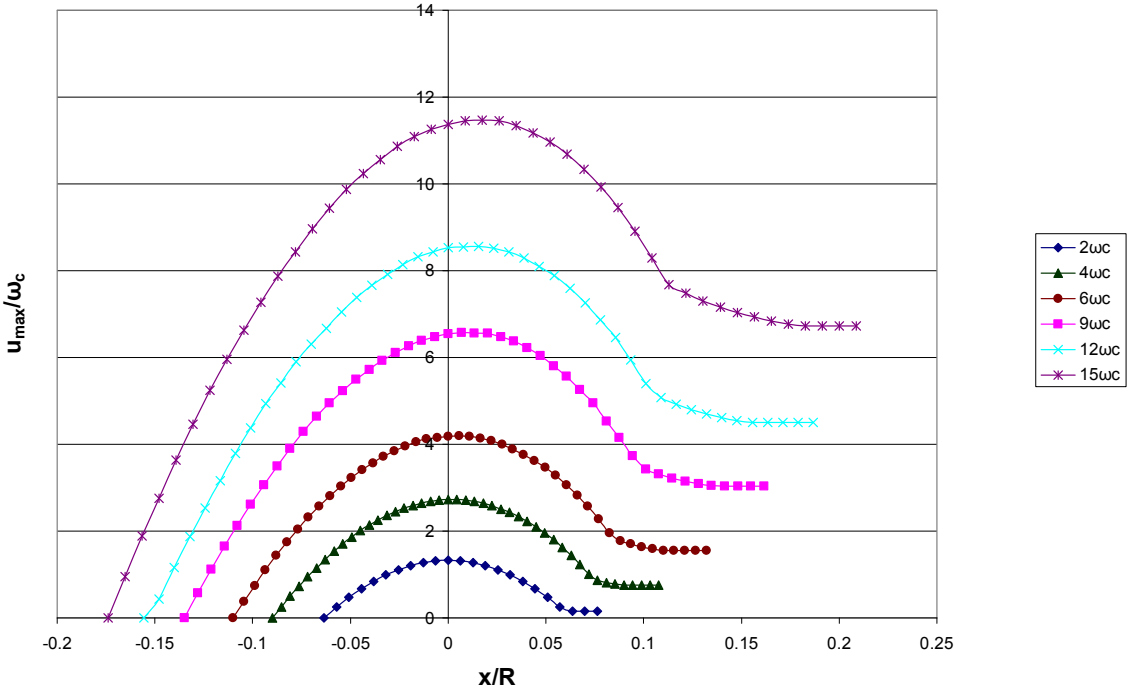

Figure 22: Normalized deformation in aluminum as sliding progresses.

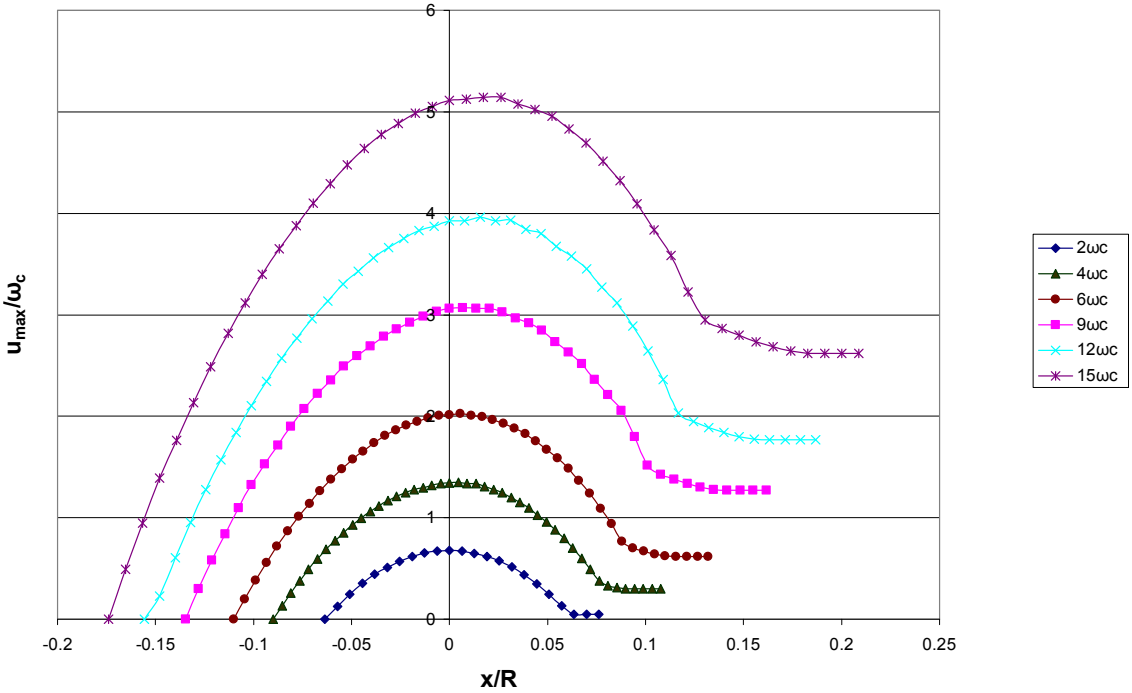

Figure 23: Normalized deformation in copper as sliding progresses.

Once the hemispheres have come out of contact they are left with residual deformation. This can be seen as a flattening out of the deformation curves in Figures 21 through 23. The simulation is run past the point when the hemispheres come out of contact in order to capture this phenomenon. This deformation is due to plasticity effects and is unrecoverable. Figure 24 presents a plot of the residual deformations in the y-direction, u_{res}, normalized by the critical interference, ω_c versus preset vertical interference, ω^*. The residual deformations dramatically increase as the interference increases. A polynomial curve fit that closely approximates the data for steel-on-steel sliding contact is given by:

$$\frac{u_{res}}{\omega_c} = 0.2(\omega^* - 1) + 0.01(\omega^* - 1)^2 \qquad 1 \le \omega^* \le 15 \qquad (15)$$

The aluminum and copper results are qualitatively similar to the steel results. However, the copper hemispheres show significantly less residual deformation. This is reasonable if one considers the fact that the copper has a higher yield strength than the aluminum such that the aluminum hemisphere will absorb most of the deformation. A polynomial curve fit for aluminum in aluminum-on-copper sliding contact is given by:

$$\frac{u_{res}}{\omega_c} = 0.248(\omega^* - 1) + 0.014(\omega^* - 1)^2 \qquad 1 \le \omega^* \le 15 \qquad (16)$$

and a curve fit for copper in aluminum-on-copper sliding contact is given by:

$$\frac{u_{res}}{\omega_c} = 0.095(\omega^* - 1) + 0.006(\omega^* - 1)^2 \qquad 1 \le \omega^* \le 15 \qquad (17)$$

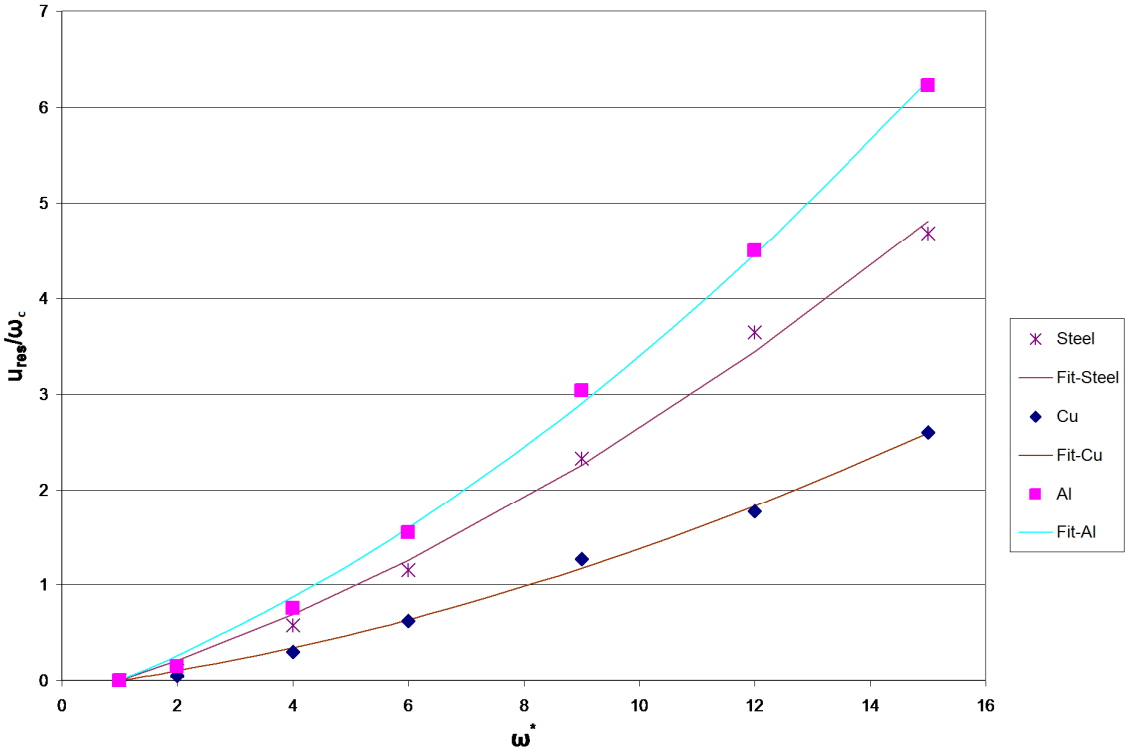

Figure 24: Normalized residual deformations versus normalized preset interference for steel-on-steel and aluminum-on-copper contact

4. Comparison to Semi-analytical Results

Elastic-plastic sliding contact has no analytical solution. This makes model verification difficult. There is, however, another numerical technique called the semi-analytical method (SAM, [33]) that can solve the said sliding problem, but it has limited capabilities regarding material composition while offering only an approximate solution at that. The purpose of this section is two-fold: (1) to compare (i.e., also verify) the results of the current FEA results with an existing solution, (2) highlight the success and limitations of SAM. A brief description of the SAM is as follows. The contact pressure on the surface can be thought of as the summation of concentrated normal loads over the contact area. Each of these concentrated loads has a corresponding influence on the

displacements throughout the body. This influence is quantified using influence coefficients, which are actually the discretized form of Green's functions. The SAM takes advantage of this by using the superposition principle to sum at each location in the region of interest the displacements due to the contact pressure. Once this information is gathered the stresses, strains, and deformations can be calculated based on the material properties from the compatibility and equilibrium relations. An iterative process is used to incorporate the residual deformations present from a previous load step [33].

Figures 25 and 26 present a comparison of the normalized horizontal and vertical reaction forces for the different vertical interferences for steel-on-steel contact, respectively. The FEA and SAM results are nearly identical for the smaller interference cases. As shown in Figure 25, with increasing preset interference, the SAM results diverge from the FEA results once the hemispheres have passed the point of vertical alignment. As the hemispheres come out of contact, the SAM predicts a higher reaction force indicating less energy loss due to plasticity. The vertical reaction force curves, as shown in Figure 26, are also nearly identical for all the interference cases presented.

One problem with the SAM as used here is that it is not capable of modeling two dissimilar materials while both being elastic-plastic. For identical materials this is not an issue (steel-on-steel for instance), but for the case of aluminum-on-copper sliding, a decision is made to model the copper hemisphere as elastic. The justification being that the residual deformations seen in the copper hemisphere are much lower than the residual deformations in the aluminum hemisphere. Figures 27 and 28 present the normalized horizontal and vertical reaction forces for aluminum-on-copper contact, respectively.

It can be seen that SAM results for both the horizontal and vertical reaction forces for the aluminum-on-copper cases, shown in Figures 27 and 28, deviate more from the FEA results than the steel-on-steel sliding cases, shown in Figures 25 and 26. The SAM produces normalized vertical reaction forces that are higher than the FEA results in the aluminum-on-copper sliding. This is due to the condition that the copper hemisphere is modeled as completely elastic resulting in a higher overall load carrying capacity. This can also be seen in the normalized horizontal reaction force curves for aluminum-on-copper contact where the SAM yields forces larger in magnitude over more of the sliding distance for the loading phase than the FEA.

Overall, the SAM method shows promise to solve these types of problems. The greatest advantage of the SAM used here is the run time. The SAM code runs only a few hours compared to days for the FEA method used. Still the SAM method cannot handle dissimilar materials, and its results show increasing deviations with increasing interferences (i.e., increasing plasticity) compared to those obtained by the FEA.

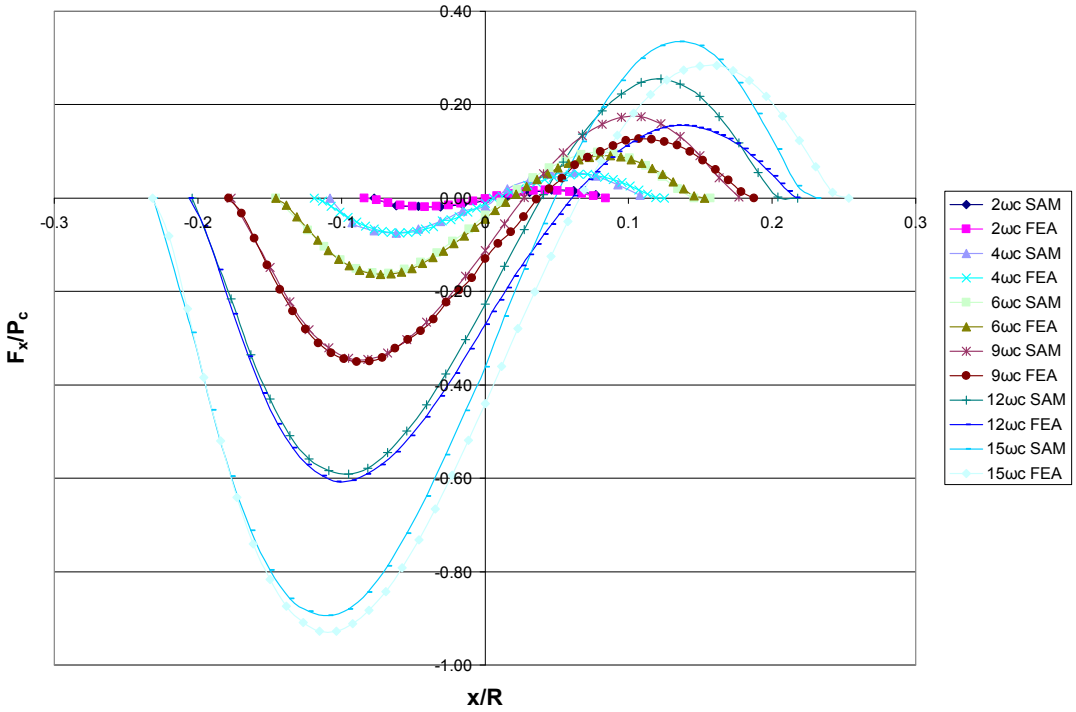

Figure 25: A comparison of the SAM and FEA results for the normalized horizontal reaction force for steel-on-steel contact.

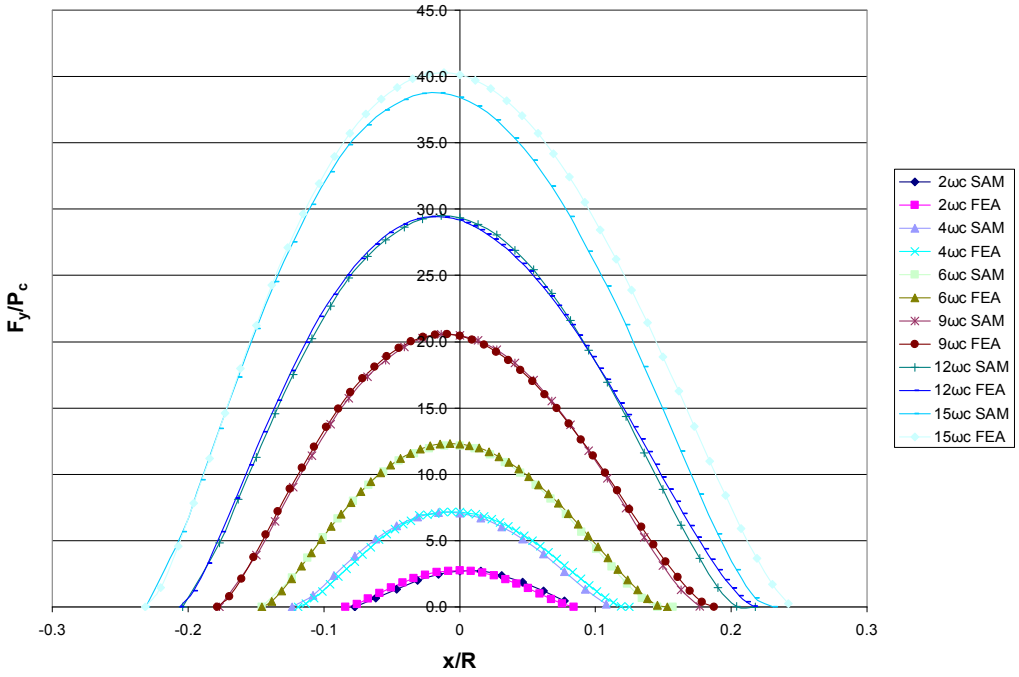

Figure 26: A comparison of the SAM and FEA results for the normalized vertical reaction force for steel-on-steel contact.

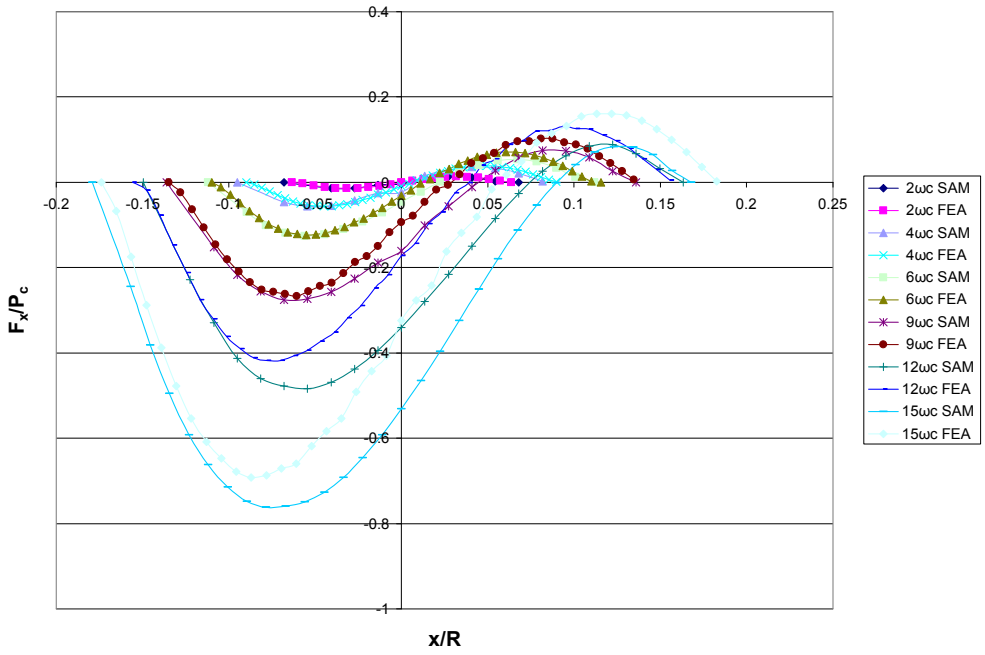

Figure 27: A comparison of the SAM and FEA results for the normalized horizontal reaction force for aluminum-on-copper contact.

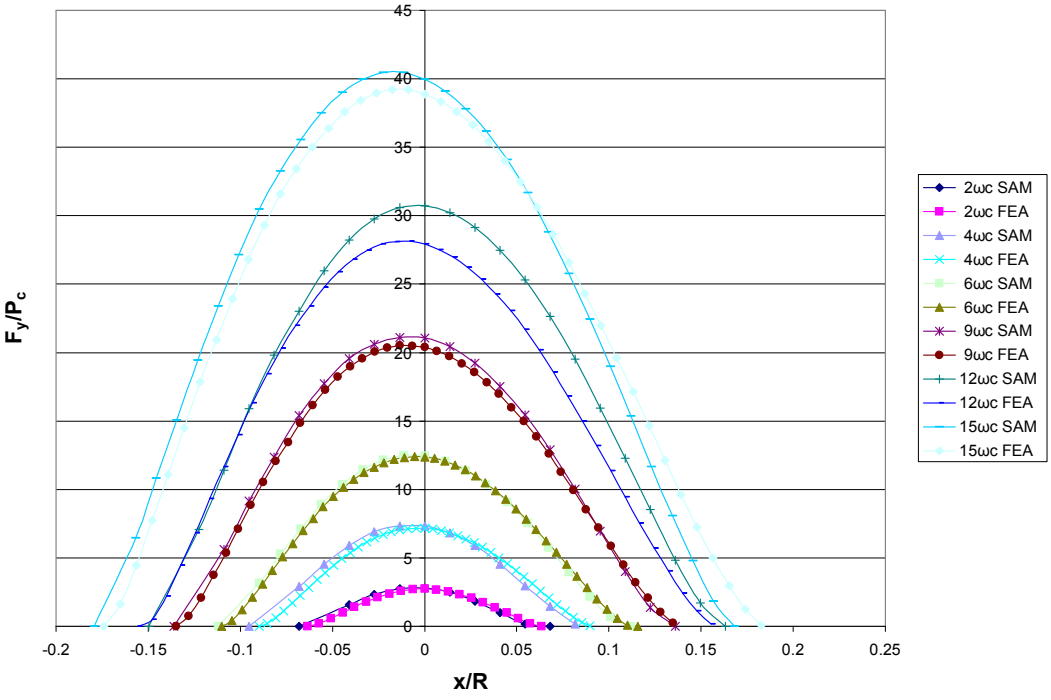

Figure 28: A comparison of the SAM and FEA results for the normalized vertical reaction force for aluminum-on-copper contact.

5: THE EFFECTIVENESS OF THE NORMALIZATION SCHEME

It has been shown that the normalization scheme, as introduced in Section 2 and defined by [22], is effective when comparing steel-on-steel and aluminum-on-copper contact. This section expands on this finding and compares the normalized reaction forces for other metal-on-metal sliding contact situations. In this section the SAM is used to model copper-on-copper, aluminum-on-aluminum, and three different steel material models for steel-on-steel sliding contact. The FEA as presented earlier is used for the aluminum-on-copper sliding contact in order to make an equitable comparison as the SAM cannot model both materials being elasto-plastic in dissimilar-material sliding contact. Table 5 presents the material properties and critical values used here.

In this analysis, a parametric study on the effects of varying the yield strength, S_y, is carried out. Since steel has a fairly constant Young's Modulus and a variable yield strength, the yield strength is varied for the parametric study. It is found that if the ratio of CS_y / E' is the same then the normalized force curves are nearly identical for identical-material contact (i.e., steel-on-steel or aluminum-on-aluminum). In fact, for the lower interference cases, it is found that the aluminum-on-copper and steel-on-steel with an identical ratio of CS_y / E' the normalized force curves are nearly identical.

Figure 29 presents the normalized horizontal reaction force versus normalized sliding distance for the materials in Table 5 for interferences of $6\omega_c$ and $15\omega_c$. As shown in the figure, the normalized force curves are nearly identical for identical-material sliding cases with the same ratio of CS_y / E'. Similar results can be seen for the steel-on-steel and aluminum-on-copper sliding cases with the same CS_y / E' ratio at a $6\omega_c$.

However, it is found that the higher interference case of the steel-on-steel and aluminum-on-copper sliding with the same CS_y / E' ratio do not match.

Figure 30 presents the normalized vertical reaction force versus normalized sliding distance. Very similar results to the normalized horizontal reaction force curves can be seen (sliding combinations with the same ratio of CS_y / E' are nearly identical). Another interesting point is that regardless of the CS_y / E' ratio, the maximum normalized vertical reaction force value is identical indicating that the critical load normalizes the maximum vertical reaction force well.

Table 5: The material properties and critical values in this comparison.

	Al-Al	Stl-Stl (1)	Cu-Cu	Stl-Stl (2)	Al-Cu	Stl-Stl (3)
P_c *[kN]*	115	346	39.5	60.4	67.3	149
E' [GPa]	38.55	111.4	72.9	111.4	50.44	111.4
C	1.645	1.637	1.65	1.637	1.645	1.637
S_y *[MPa]*	310	911.1	310	505	310	687.9
ω_c *[mm]*	0.216	0.221	0.0691	0.0691	0.126	0.126
CSy/E'	0.013	0.013	0.007	0.007	0.01	0.01

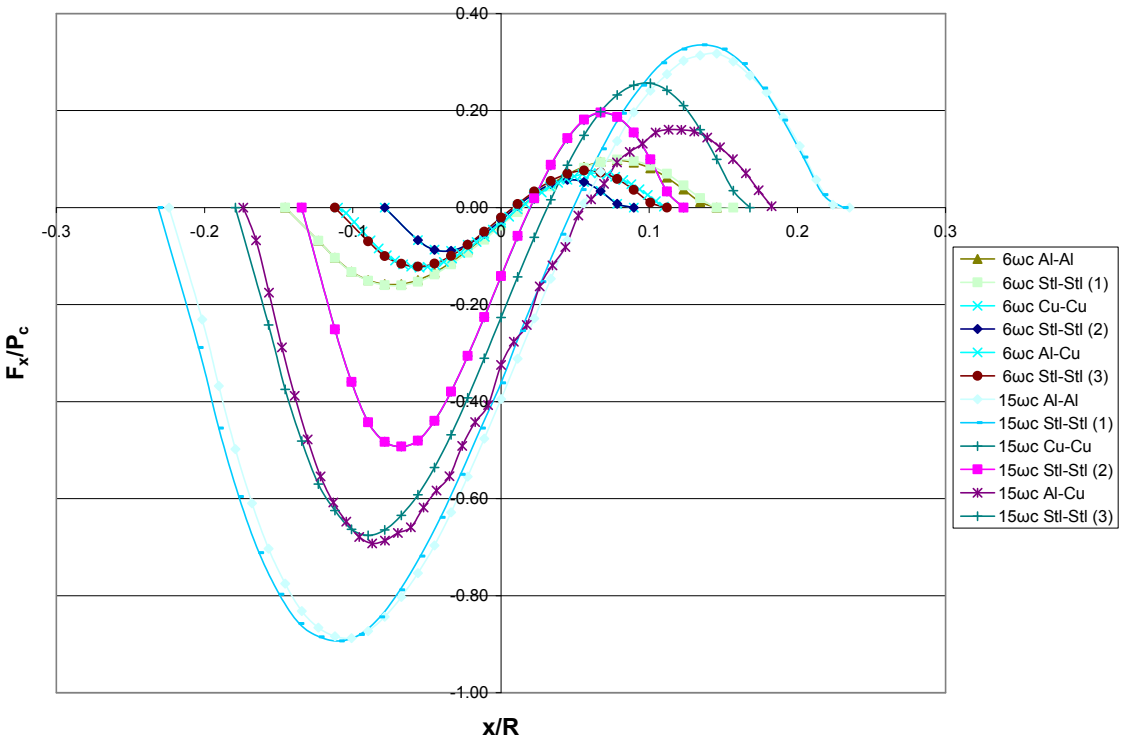

Figure 29: Normalized horizontal reaction force versus normalized sliding distance.

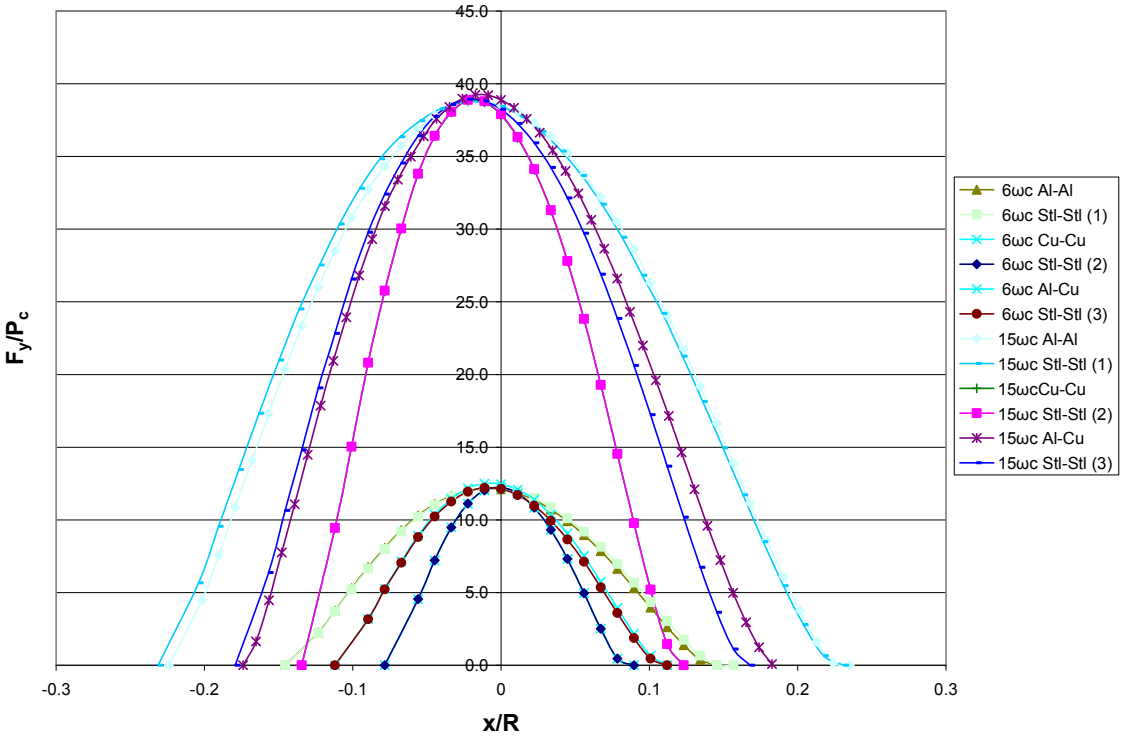

Figure 30: Normalized horizontal reaction force versus normalized sliding distance.

6. Conclusions

The results of the FEA of frictionless sliding in the elastic-plastic domain between two hemispheres are discussed. Results are presented for sliding between two steel hemispheres and between an Al and a Cu hemisphere. The resultant parameters such as deformations, forces, stresses, and energy losses that occur are presented and explained. All the results are presented nondimensionally in order to apply to hemispherical contact at any scale. The development and propagation of stress in the hemispheres as sliding progresses is discussed. It is found that as the interference increases, the stresses in the hemispheres expand and reach the surface at values slightly above the yield strength. The reaction forces required to maintain straight line contact are investigated and a "load ratio" is defined, similar to a friction coefficient due to mechanical interference only. A single set of equations is derived to characterize the energy loss due to plastic deformation in both cases because it is found that the magnitudes of the net energy at the end of sliding are similar for all cases analyzed. An effective coefficient of friction is introduced in order to help quantify energy loss due to plasticity. Equations to characterize residual deformations in steel-on-steel contact and aluminum-on-copper contact are derived. It is shown that aluminum shows more deformation than copper throughout the progression of sliding. Contact areas during sliding are presented and it is also found that the normalized dimensions of the contact region are larger in aluminum-on-copper contact.

The FEA results are compared against a semi-analytical method (SAM). The FEA and SAM results are nearly identical for the smaller interference cases. With increasing preset interference, the SAM results diverge from the FEA results once the hemispheres

have passed the point of vertical alignment. As the hemispheres come out of contact, the SAM predicts a higher horizontal reaction force indicating less energy loss due to plasticity. The vertical reaction force curves are nearly identical for both FEA and SAM for all the interference cases presented.

The SAM results for both the horizontal and vertical reaction forces for the aluminum-on-copper cases deviate more from the FEA results than the steel-on-steel sliding cases. This is because the SAM code in its current state cannot model both hemispheres as elastic-plastic, and hence the Cu is assumed elastic throughout. The SAM produces normalized vertical reaction forces that are higher than the FEA results in the aluminum-on-copper sliding. This is due to the condition that the copper hemisphere is modeled as completely elastic resulting in a higher overall load carrying capacity.

A parametric study on the effectiveness of the normalization scheme is carried out. It is found that if the ratio of CS_y / E' is the same then the normalized reaction force curves are nearly identical for identical-material contact. This result can also be seen in the lower interference cases of dissimilar-material contact situations with the same ratio of CS_y / E', though the results diverge as the interference increases. It is also found that regardless of the CS_y / E' ratio the maximum normalized vertical reaction force value is identical indicating that the critical load normalizes the maximum vertical reaction force well regardless of the material combination.

References

1. Liu, G., Q.J. Wang, and C. Lin, A Survey of Current Models for Simulating the Contact between Rough Surfaces. Tribology Transactions, 1999. 42: p. 581-591.

2. Thomas, T.R., Rough Surfaces. Imperial College Press,1982.

3. Greenwood, J.A., A unified Theory of Surface Roughness. Proceedings of the Royal Society of London, A, 1984. 393: p. 133-157.

4. Greenwood, J.A. and J.B.P. Williamson, Contact of Nominally Flat Surfaces. Proceedings of the Royal Society of London. Series A, Mathematical and Physical Sciences, 1966. 295(1442): p. 300-319.

5. Bush, A.W., R.D. Gibson, and T.R. Thomas, The Elastic Contact of Rough Surfaces. Wear, 1975. 35: p. 87-111.

6. Greenwood, J.A. and J.H. Tripp, The Elastic Contact of Rough Spheres. ASME Trans., Journal of Applied Mechanics, 1967. 34: p. 153-159.

7. Lo, C.C., Elastic Contact of Rough Cylinders. Int. J. Mech. Sci., 1969. 11: p. 105-115.

8. Tsukizoe, T. and T. Hisakado, On the Mechanism of Contact between Metal Surfaces: Part 2 - The Real Area and the Number of Contact points. ASME Journal of Lubrication Tribology, 1968. F90: p. 81-90.

9. Whitehouse, D.J. and J.F. Archard, The Properties of Random Surface of Significance in their Contact. Proceedings of the Royal Society of London, A316, 1970: p. 97-121.

10. Abbot, E.J. and F.A. Firestone, Specifying Surface Quality - A Method Based on Accurate Measurement and Comparison. Mechanical Engineering, 1933. 55: p. 569.

11. Evseev, D.G., B.M. Medvedev, and G.G. Grigoriyan, Modification of the Elastic-Plastic Model for the Contact of Rough Surfaces. Wear, 1991. 150: p. 79-88.

12. Chang, W.R., An Elastic-Plastic Contact Model for a Rough Surface with an Ion-Plated Soft metallic Coating. Wear, 1997. 212: p. 229-237.

13. Zhao, Y.W., An Asperity Microcontact Model Incorporating the Transition from Elastic Deformation to Full Plastic Flow. ASME Trans.,Journal of Tribology, 2000. 122: p. 86-93.

14. Vu-Quoc, L., X. Zhang, and L. Lesburg, A Normal Force-Displacement Model for Contacting Spheres Accounting for Plastic Deformation: Force-Driven Formulation. ASME Journal of Applied Mechanics, 2000. 67: p. 363-371.

15. Nosonovsky, M. and G.G. Adams, Steady-state frictional sliding of two elastic bodies with a wavy contact interface. ASME Trans., Journal of Tribology, Transactions of the ASME, 2000. 122(3): p. 490.

16. Jackson, R., I. Chusoipin, and I. Green, A Finite Element Study of the Residual Stress and Deformation in Hemispherical Contacts. ASME Trans., Journal of Tribology, 2005. 127(3): p. 484.

17. Wang, F. and L.M. Keer, Numerical simulation for three dimensional elastic-plastic contact with hardening behavior. ASME Trans., Journal of Tribology, 2005. 127(3): p. 494.

18. Green, A.P., The plastic yielding of metal junctions due to combined shear and pressure. Journal of Mechanics and Physical Solids, 1954. 2: p. 197-211.

19. Green, A.P., Friction between unlubricated metals: a theoretical analysis of the junction medel. Proceedings of the Royal Society, 1955: p. 191-204.

20. Faulkner, A. and R.D. Arnell, The development of a finite element model to simulate the sliding interaction between two, three-dimensional, elastoplastic, hemispherical asperities. Wear, 2000. 242(1-2): p. 114.

21. Jackson, R.L., et al., An analysis of elasto-plastic sliding spherical asperity interaction. Wear, 2007. 262(1-2): p. 210-219.

22. Leonard, B. D., Sadeghi, F., Evans, R. D., Doll, G. L., and Shiller, P. J., 2009, "Fretting of WC/aC: H and Cr2N coatings under grease-lubricated and unlubricated conditions," Tribology Transactions, 53(1), pp. 145-153.

23. Leonard, B. D., Sadeghi, F., Shinde, S., and Mittelbach, M., 2012, "A novel modular fretting wear test rig," Wear, 274, pp. 313-325.

24. Warhadpande, A., Leonard, B., and Sadeghi, F., 2008, "Effects of fretting wear on rolling contact fatigue life of M50 bearing steel," Proceedings of the Institution of Mechanical Engineers, Part J: Journal of Engineering Tribology, 222(2), pp. 69-80.

25. Leonard, B., Sadeghi, F., and Cipra, R., 2008, "Gaseous cavitation and wear in lubricated fretting contacts," Tribology Transactions, 51(3), pp. 351-360.

26. Kogut, L., and Etsion, I., 2002, "Elastic-plastic contact analysis of a sphere and a rigid flat," ASME J. Appl. Mech, 69(5), pp. 657-662.

27. Jackson, R. L., and Green, I., 2005, "A finite element study of elasto-plastic hemispherical contact against a rigid flat," Transactions of the ASME, Journal of Tribology, 127(2), pp. 343-354.

28. Tsukizoe, T., and Hisakado, T., 1968, "On the Mechanism of Contact Between Metal Surfaces: Part 2-The Real Area and the Number of the Contact Points," Journal of Lubrication Technology, 90(1), pp. 81-88.

29. Sharma, A., and Jackson, R. L., 2017, "A Finite Element Study of an Elasto-Plastic Disk or Cylindrical Contact Against a Rigid Flat in Plane Stress with Bilinear Hardening," Tribology Letters, 65(3), p. 112.

30. Brizmer, V., Kligerman, Y., and Etsion, I., 2007, "A model for junction growth of a spherical contact under full stick condition," Journal of Tribology, 129(4), pp. 783-790.

31. Chang, L., and Zhang, H., 2007, "A mathematical model for frictional elastic-plastic sphere-on-flat contacts at sliding incipient," Journal of Applied Mechanics, 74(1), pp. 100-106.

32. Vijaywargiya, R., and Green, I., 2007, "A finite element study of the deformations, forces, stress formations, and energy losses in sliding cylindrical contacts," International Journal of Non-Linear Mechanics, 42(7), pp. 914-927.

33. Boucly, V., et al. “Modeling of the Rolling and Sliding contact Between Two Asperities,” ASME Trans., Journal of Tribology, 2007. Vo. 129, No. 2, (April 2007), 235-245.

34. Gupta, V., Bastias, P., Hahn, G. T., and Rubin, C. A., 1993, "Elasto-plastic finite-element analysis of 2-D rolling-plus-sliding contact with temperature-dependent bearing steel material properties," Wear, 169(2), pp. 251-256.

35. Ghosh, A., Leonard, B., and Sadeghi, F., 2013, "A stress based damage mechanics model to simulate fretting wear of Hertzian line contact in partial slip," Wear, 307(1), pp. 87-99.

36. Zolotarevskiy, V., Kligerman, Y., Etsion, I. Elastic-plastic spherical contact under cyclic tangential loading in pre-sliding. Wear, 2011, 270, 11-12: p. 888-894

37. Huaidong, Y., and Green, I., "An Elasto-Plastic Finite Element Study of Displacement-Controlled Fretting in a Plane-Strain Cylindrical Contact," Accepted for publication, ASME Trans., Journal of Tribology, (December 2017), TRIB-17-1391, doi:10.1115/1.4038984.

38. Green, I., “Poisson Ratio Effects and Critical Values in Spherical and Cylindrical Hertzian Contacts,” International Journal of Applied Mechanics, 2005. 10(3): p. 451-462.